Reports on Progress in Physics

REPORT ON PROGRESS

Quantum imaging and information

To cite this article: Omar S Magaña-Loaiza and Robert W Boyd 2019 *Rep. Prog. Phys.* **82** 124401

View the article online for updates and enhancements.

IOP ebooks™

Bringing you innovative digital publishing with leading voices to create your essential collection of books in STEM research.

Start exploring the collection - download the first chapter of every title for free.

This content was downloaded from IP address 137.122.64.31 on 20/11/2019 at 20:29

IOP Publishing

Reports on Progress in Physics

Rep. Prog. Phys. **82** (2019) 124401 (28pp)

https://doi.org/10.1088/1361-6633/ab5005

Report on Progress

Quantum imaging and information

Omar S Magaña-Loaiza[1] and Robert W Boyd[2]

[1] Department of Physics and Astronomy, Louisiana State University, Baton Rouge, LA 70803, United States of America
[2] Institute of Optics, University of Rochester, Rochester, NY 14627, United States of America

E-mail: maganaloaiza@lsu.edu

Received 28 January 2019, revised 25 August 2019
Accepted for publication 22 October 2019
Published 19 November 2019

Corresponding Editor Professor Masud Mansuripur

Abstract

The maturity of fields such as optical physics and quantum optics has brought with it a new era where the photon represents a promising information resource. In the past few years, scientists and engineers have exploited multiple degrees of freedom of the photon to perform information processing for a wide variety of applications. Of particular importance, the transverse spatial degree of freedom has offered a flexible platform to test complex quantum information protocols in a relatively simple fashion. In this regard, novel imaging techniques that exploit the quantum properties of light have also been investigated. In this review article, we define the fundamental parameters that describe the spatial wavefunction of the photon and establish their importance for applications in quantum information processing. More specifically, we describe the underlying physics behind remarkable protocols in which information is processed through high-dimensional spatial states of photons with sub-shot-noise levels or where quantum images with unique resolution features are formed. We also discuss the fundamental role that certain imaging techniques have played in the development of novel methods for quantum information processing and vice versa.

Keywords: imaging, quantum information, light, quantum optics, optical physics, quantum measurement, quantum communication

(Some figures may appear in colour only in the online journal)

1. Introduction

The control of photons represents a pillar of our modern technological society. The emerging field of quantum photonics exploits quantum properties of light to dramatically improve the performance of protocols for communication, metrology, imaging and information processing [1–4]. These remarkable examples of photonic technologies have been demonstrated through the precise manipulation of polarization and the spectral and spatial properties of photons. The possibility of engineering complex optical fields with specific polarization properties, phases or values of orbital angular momentum (OAM) at specific transverse locations has allowed scientists to utilize the transverse degree of photons to develop novel paradigms in quantum photonic technologies that go beyond optical imaging [1–4].

In the past few years, there has been a strong impetus to develop methods to infer amplitude and phase information of optical fields for various applications, ranging from astrophysics to medical sciences [5–12]. These techniques, that utilize interferometry, wavefront sensing and projective measurements to characterize the spatial degree of freedom of light, have been applied to quantum protocols for information processing [3, 7–13]. The similarities existing among certain protocols for quantum information science and quantum imaging have triggered a rapid evolution of both fields [2].

© 2019 IOP Publishing Ltd Printed in the UK

In this review article, we introduce the fundamental physics behind these two important forms of quantum technologies and describe the challenges that both disciplines face.

The next section of this article is devoted to the description of the spatial properties of light and how these can be used to define complex superpositions and high-dimensional Hilbert spaces. This section is followed by a description of spatial correlations in the degrees of freedom of linear position, linear momentum, angular position (ANG) and OAM. The third and fourth sections of this article introduce the basic ideas behind correlated imaging and compressive sensing (CS), respectively. A discussion regarding the relevance of high-dimensional spatial states for quantum measurement theory is presented in the fifth section. The last section is devoted to discuss interesting connections between quantum imaging and quantum information science. We conclude our review by providing the reader with the most representative challenges in the fields of quantum imaging and quantum information science.

2. The transverse profile of light and spatial wavefunctions

The underlying mathematical structure of wave theories has allowed physicists to establish interesting connections that have led to interesting philosophical discussions in physics [14, 15]. More specifically, the similarities between electromagnetic theory and quantum mechanics have motivated investigations regarding the existence of the wavefunction of a photon and its relationship with the transverse degree of freedom of the electromagnetic field [7, 14, 15]. Interestingly, in the context of optical physics, there has been extensive research work devoted to the measurement of the real and imaginary components of the electromagnetic field [16, 17]. Similarly, in the quantum domain, the measurement of the real and imaginary parts of the photonic wavefunction has been performed by means of quantum state tomography [7, 8, 18]. In this regard, there has been a strong interest in engineering fundamental properties of photonic wavefunctions to perform tasks for quantum imaging and information processing [19]. In this section, we will describe fundamental properties of light that can be used to define photonic wavefunctions.

2.1. Linear and spin angular momentum of photons

The identification of the linear momentum of light can be traced back to the seventeenth century when Johannes Kepler suggested that radiation pressure from the sun played an important role in defining the orientation of comet tails. This seminal idea influenced scientists and philosophers to explore mysteries surrounding the nature of light [20]. However, it was not until the end of the nineteenth century and the beginning of the twentieth that the formulation of the electromagnetic theory of light and the development of quantum mechanics allowed the theoretical description of electromagnetic momentum. The formulation of Maxwell equations in free-space allows the definition of the density of the linear momentum $\hat{P}_k$ as

$$\hat{P}_k = \frac{\hat{E} \times \hat{H}}{c^2}, \tag{1}$$

where c represents the speed of light in vacuum and the electric and magnetic fields are described by the vectors $\hat{E}$ and $\hat{H}$, respectively. Thus, the magnitude for density of linear momentum can be written in terms of the energy density U as

$$P_k = \frac{U}{c}. \tag{2}$$

Consequently, by making use of the energy carried by a single photon, $\hbar\omega$, it is possible to express the momentum per photon as

$$\hat{p} = \hbar\hat{k}. \tag{3}$$

The magnitude of the wavevector $|\hat{k}|$ is defined as $2\pi/\lambda$, where λ represents the wavelength of the photon. The wavevector provides information about the spatial frequency of the photon. The properties of the photons in the position and momentum domains enable the full spatial description of an optical field [19]. Even though the mathematical definition of photon momentum might look abstract at first glance, the wavevector typically defines the direction of propagation. In practice, the photon wavevector can be measured using a simple experimental setup, such as the one depicted in figure 1. In this case, the spatial distribution of photons, in the aperture plane, is described by the transverse wavefunction $\psi(\hat{x})$. Naturally, this is defined by the geometry of the aperture. The corresponding momentum distribution of the transmitted photons can be found by performing a Fourier transform operation. This transformation can be implemented using a lens, thus, the intensity distribution in the far-field is described by $|\psi(\hat{k})|^2$. As illustrated in figure 1, photons with different spatial frequency components, and thus different linear momentum components, hit specific locations on the screen located in the Fourier plane of the lens. As discussed below, it is possible to engineer the phase of light beams at specific transverse positions to produce complex wavefunctions with exotic distributions of linear momentum [8]. These structured beams have been utilized for applications in optical imaging and optical communications [3, 19].

In addition to linear momentum, photons can carry spin angular momentum. The angular momentum of light has been utilized to implement photonic qubits in protocols for quantum information processing [21]. The rotation of the electric field with respect to the propagation direction defines the spin angular momentum of light, see figures 2(a) and (b). In 1936, Beth reported the first experimental observation of the angular momentum of light associated with the polarization of a light beam [22]. In his landmark experiment, he observed a mechanical torque on a qurtz plate. The measured torques were in the order of 10^{-9} dyne cm. As shown in figures 2(a) and (b), circularly polarized light is characterized by a symmetric rotation of the electric field. In this case,

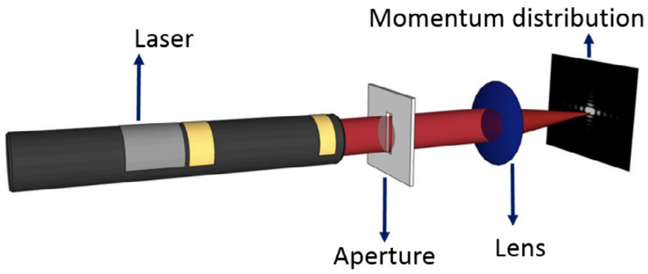

Figure 1. The concept of spatial frequency components and linear momentum of light are introduced in the context of diffraction. The intensity distribution formed in the Fourier plane of the lens reveals different spatial frequency components that indicate the presence of different photon wavevectors.

each photon with circular polarization carries spin angular momentum given by $\sigma\hbar$. The spin angular momentum can be positive or negative, for example, σ is equal to -1 for left-handed circular polarized light and to $+1$ for right-handed. These polarization states of a photon are eigenstates of the spin operator. As discussed below, polarization states of light have been utilized to encode quantum bits of information in single photons [23, 24].

2.2. OAM

In addition to linear and spin angular momentum, light can also carry OAM [25]. The OAM of light is due to a helical phase front given by an azimuthal phase dependence of the form $e^{i\ell\phi}$, where ℓ represents the OAM number and ϕ represents the azimuthal angle [26]. In general these beams have the following mathematical form

$$E(x,y,z,\phi) = u_0(x,y,z)e^{ikz}e^{-i\ell\phi} \tag{4}$$

which describes a beam of light with a slowly varying amplitude distribution $u_0(x, y, z)$ propagating along the z coordinate. Optical beams with these properties are solutions to the paraxial approximation of the Helmholtz equation, which is written in a Cartesian coordinate system as

$$[\frac{\partial^2}{\partial x^2} + \frac{\partial^2}{\partial y^2} + 2ik\frac{\partial}{\partial z}]u_0(x,y,z) = 0. \tag{5}$$

This equation is satisfied by cylindrical Laguerre–Gauss modes $LG_p^\ell(\rho,\phi,z)$, which consist of a family of orthogonal modes that have well defined values of OAM. The field amplitude of a normalized Laguerre–Gauss mode is given by

$$LG_p^\ell(\rho,\phi,z) = \sqrt{\frac{2p!}{\pi(|\ell+p|)!}}\frac{1}{w(z)}\left[\frac{\sqrt{2}\rho}{w(z)}\right]^{|\ell|}L_p^\ell\left[\frac{2\rho^2}{w^2(z)}\right]$$
$$\exp\left[-\frac{\rho^2}{w^2(z)}\right]\exp\left[-\frac{ik^2\rho^2 z}{2(z^2+z_R^2)}\right]$$
$$\exp\left[i(2p+|\ell|+1)\right]\tan^{-1}\left(\frac{z}{z_R}\right) \tag{6}$$

where p is the radial index, $w(z)$ is the beam waist given by $\sqrt{2(z^2+z_R^2)/k_{z_R}}$, z_R is the Rayleigh range defined as $kw^2(0)/2$, $L_p^{|\ell|}$ is the associated Laguerre polynomial and ρ, ϕ denote the transverse coordinates. Each photon in a Laguerre–Gaussian mode carries an OAM $\ell\hbar$. The azimuthal phase dependence of these beams induces the helical phase fronts shown in figures 2(c) and (d).

There are different methods in which beams carrying OAM can be generated and detected [25]. Most of the work presented in this review makes use of computer generated holograms, digital micro-mirror devices (DMDs) and spatial light modulators (SLMs) [27]. The encoded holograms contain the phase information that endows light with OAM and a diffraction grating that allows one to increase the quality of the generated modes. As shown in figure 3(a), a SLM and a lens allows one to select a diffracted beam that carries specific values of OAM. Interestingly, the exact same technique can be used in reverse to characterize the OAM spectrum of light, see figure 3(b). The fact that the singularity of a beam carrying OAM can be removed by projecting it onto the conjugate azimuthal phase allows one to determine the OAM spectrum of light. In figure 3(b) a beam of light carrying a specific value of OAM is projected onto $-\ell$, this produces a Gaussian mode, which is the only mode that couples efficiently onto a single mode fiber. If the beam is projected onto a different mode, then only a small amount of light is coupled to the fiber. In general, this procedure allows for the determination of the OAM spectrum of light.

As described below, beams of light carrying OAM have not only played an important role in the understanding of fundamental properties of light but also in the development of novel photonic technologies [3, 25]. Interestingly, there has been an enormous interest in using the OAM of light for implementing functional protocols for communication, cryptography, imaging, metrology, particle manipulation and, in general, information processing [28]. In the next sections we outline some of the major motivations behind some of the most remarkable OAM protocols.

2.3. High-dimensional photonic states

The polarization of photons is one of their multiple properties that can be used to encode quantum bits of information, typically known as qubits [23, 24]. In the degree of freedom of polarization, a single photon can be measured in one of two mutually exclusive polarization states, for example, the polarization state can be circular to the left or circular to the right. In the standard Dirac notation, this can be described as $|L\rangle$ and $|R\rangle$, respectively. However, a generic pure polarization state can be described as follows

$$|\psi\rangle = a|L\rangle + b|R\rangle, \tag{7}$$

for a normalized state, the complex coefficients a and b satisfy

$$|a|^2 + |b|^2 = 1. \tag{8}$$

The state $|\psi\rangle$ in equation (7) represents a qubit with the circular polarization states of light acting as the representation basis. The coefficients in the wavefunction $|\psi\rangle$ can be carefully prepared to produce specific probabilities of measuring the state in one of the two polarizations. This process is known as state preparation. The probability of measuring a photon in the circular to the left state is simply given by the squared amplitude

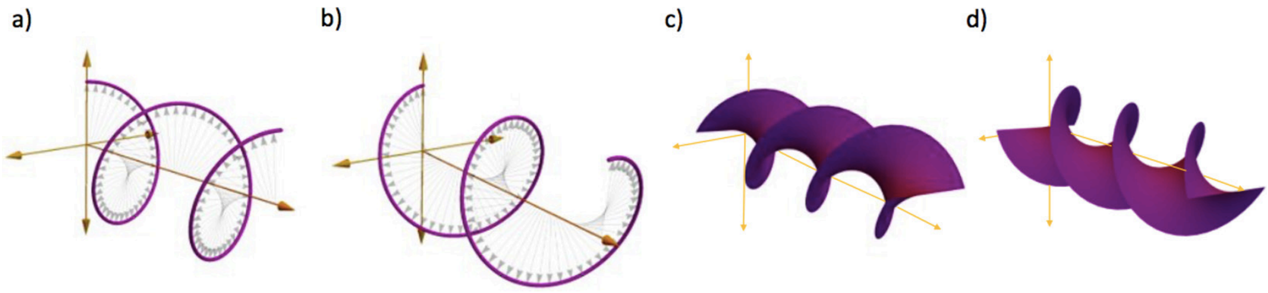

Figure 2. The rotation of the electric field and the helical phase fronts of photons define the total angular momentum of light. The spin angular momentum of light is caused by the circular polarization of photons, the rotation of the electric field for right-handed circular polarized light is shown in (a), the rotation for left-handed circular polarized light is shown in (b). The helical phase front for a beam of light with a positive value of OAM, $\ell = 3$ is shown in (c), a beam of light with a negative value of OAM is shown in (d), in this case $\ell = -3$.

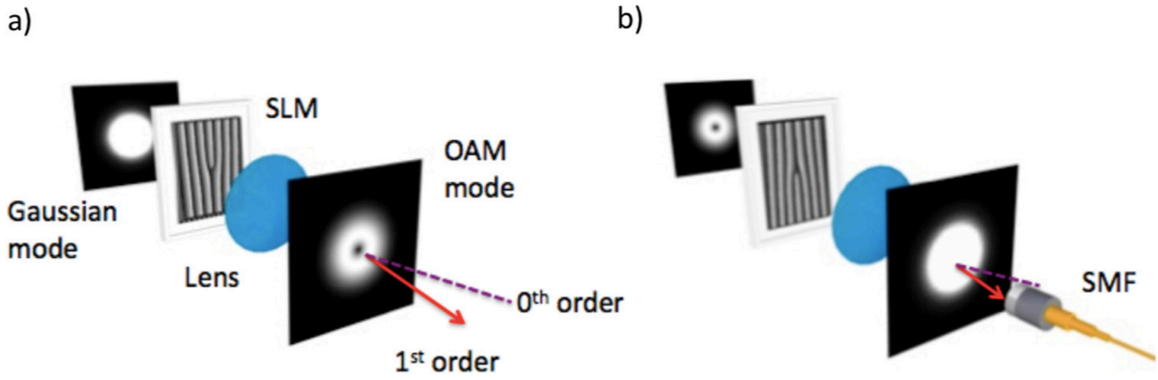

Figure 3. Generation and detection of beams of light carrying OAM. (a) shows a spatial light modulator (SLM) displaying a computer-generated hologram that allows one to generate beams of light carrying specific values of OAM. The engineered mode is selected from the first diffraction order in the Fourier plane of the SLM. As shown in (b) a similar forked diffraction grating displayed onto the SLM can also be utilized to measure the OAM spectrum of light.

of the complex coefficient a, this is $P_a = |a|^2$. Similarly, the probability of finding a photon in the circular to the right state is given by $P_b = |b|^2$. In practice, one can obtain this information by performing projective measurements, in this case, the projective operators can be defined as

$$\hat{P}_L = |L\rangle\langle L| \text{ and } \hat{P}_{\mathrm{R}} = |R\rangle\langle R|. \quad (9)$$

The probability of measuring a photon, that has been prepared in the state $|\psi\rangle$, in a circular to the left state is given by the expectation value of the projector operator $\hat{P}_L$

$$p_L = \langle\psi|\hat{P}_L|\psi\rangle = |\langle\psi|L\rangle|^2. \quad (10)$$

Alternatively, one can prepare the initial state in either $|L\rangle$ or $|R\rangle$ and this system can be projected onto the operators in equation (9). In this case, it is possible to infer the initial state with 100% certainty. In addition, one can assume that a photon is prepared in left circular polarization, $|L\rangle$. Then, one can mathematically project this state onto the new set of basis $|P_\pm\rangle$ defined as

$$|P_\pm\rangle = \frac{1}{\sqrt{2}}(|L\rangle \pm |R\rangle). \quad (11)$$

If this mathematical projection also corresponds to a physical measurement, then one would find the photon in the state $|P_+\rangle$ or $|P_-\rangle$ with 50% of probability.

The polarization properties of photons allows one to define a two-dimensional (2D) Hilbert space that has resulted fundamentally important for many applications in quantum information science [23, 24]. In general, it is possible to define a set of conjugate basis for any Hilbert space, these basis are known as mutually unbiased basis (MUBs). The use of MUBs allows the characterization of a state in a given basis system by performing a series of projections in the conjugate basis. Thus, the projections of a state onto its MUBs lead to equal detection probabilities among all states that form the conjugate basis. In this regard, the outcome of the projective measurement is completely random and unbiased. Sharing similarities with conjugate variables such as position and momentum, the multiple MUBs that one can define using polarization qubits can be related through discrete Fourier transforms. Consequently, the polarization MUBs form discrete conjugate basis. By construction, this is a general result that remains valid for other degrees of freedom of light such as OAM. This implies that for any set of general states,

$$|\langle\alpha|\beta\rangle|^2 = 1/N \quad (12)$$

where $|\alpha\rangle$ and $|\beta\rangle$ are two general states from different MUBs and N represents the dimensionality of the Hilbert space. For example, the polarization properties of a photon can also be described in terms of its horizontal and vertical polarization components. However, one can also chose an additional sets of basis, for instance, the polarization state of a photon can also be described in terms of diagonal or anti-diagonal polarization states. As shown below, the horizontal and vertical polarization states can be expressed in terms of the circular polarization states

$$|H\rangle = \frac{1}{\sqrt{2}}(|R\rangle + |L\rangle) \tag{13}$$

$$|V\rangle = \frac{\mathrm{i}}{\sqrt{2}}(|R\rangle - |L\rangle). \tag{14}$$

In the degree of freedom of polarization, the projections on the MUBs lead to

$$|\langle R|H\rangle|^2 = |\langle R|V\rangle|^2 = |\langle R|D\rangle|^2 = |\langle R|A\rangle|^2 = 1/2. \tag{15}$$

In this case, $|D\rangle$ and $|A\rangle$ represent diagonal and anti-diagonal polarization states, respectively. These projections unveil the dimensionality of the Hilbert space. Each projection provides the same information about the circularly polarized state $|R\rangle$. The projections onto the states that define the MUBs are widely used in protocols for quantum state tomography and quantum information science [2, 23].

Interestingly, one can exploit other degrees of freedom of photons to prepare complex superpositions of more than two states. In addition, it is possible to define high-dimensional MUBs. These ideas can be implemented by utilizing the frequency spectrum of photons, linear momentum, OAM and the excitation mode of the field [29–34]. In the basis of OAM, one can for example define a high-dimensional photonic wavefunction in the following form

$$|\phi\rangle = \frac{1}{\sqrt{5}}(|\ell=-2\rangle + |\ell=-1\rangle + |\ell=0\rangle + |\ell=1\rangle + |\ell=2\rangle). \tag{16}$$

Alternatively, it is also possible to define a high-dimensional set of MUBS as shown below

$$\Phi = \frac{1}{\sqrt{5}} \sum_{\ell=-5}^{\ell=5} \Phi_{\mathrm{OAM}}^{\ell} \exp\left(\mathrm{i}\frac{2\pi n\ell}{5}\right). \tag{17}$$

The coefficient $\Phi_{\mathrm{OAM}}^{\ell}$ represents a spatial mode with a top-hat intensity distribution and a helical phase profile given by the azimuthal phase dependence $\mathrm{e}^{\mathrm{i}\ell\phi}$. In this case, one can obtain the same amount of information from the state $|\Phi\rangle$ by projecting it onto different OAM values $|\ell\rangle$

$$|\langle\Phi|\ell\rangle|^2 = 1/5 \tag{18}$$

as before, the denominator in equation (18) represents the dimensionality of the Hilbert space. In contrast to other degrees of freedom, such as the excitation mode of the field, the relative simplicity of experimental methods utilized to prepare high-dimensional OAM states has made the OAM of light an attractive tool for quantum imaging and quantum information science [3, 25, 28].

2.4. The information content of a photon

The interest and motivation behind encoding information in high-dimensional photonic states is discussed in this section. We describe basic ideas and concepts from information theory that are necessary to understand recent research related to the information content of the photon [3, 25, 28].

In 1948, Claude Shannon founded the field of classical information theory with his seminal paper entitled ‘A mathematical theory of communication’ [36]. His contributions not only changed the field of communication but modern science [37]. His groundbreaking work applied probability theory to understand limits of communication and to quantify information [38]. His beautiful theory enabled him to quantify information through binary digits known as bits of information, classical probabilities and entropies [36]. Notably, it is possible to associate concepts from Shannon’s information theory with common situations in our everyday life. In a practical context, one bit of information is given by the information obtained in the answer of a yes/no question. For example, the concept of bit of information can be illustrated with the results in a coin tossing game. As dictated by common experience, it is not possible to predict the outcome of a fair flip coin. However, it is possible to gain one bit of information about this random process by asking the result of the coin toss. Furthermore, we should consider a situation in which the coin is not fair, and the probability of ‘tails’ is higher than the probability of ‘heads’. In this case, the probability of ‘guessing’ the outcome is higher. Consequently, one would gain less information by asking the result of the coin flip. Interestingly, the surprise involved in the previous situations and in yes/no questions was quantified by Shannon through entropy. Thus, the entropy associated to the toss of a fair coin is higher than the entropy that characterizes the toss of an unfair coin. This means that one gains more information through the answer of yes/no questions for the fair coin toss. These ideas constitute the pillars of modern communication [36, 38, 39].

We utilize the polarization degree of freedom of light to illustrate basic concepts that allows one to describe the simplest scheme for photonic encoding of information. We start this section by describing the potential of the polarization states in equations (13) and (14) for information encoding. The information capacity of a photon in these states can be analyzed by utilizing the concept of Shannon entropy [38]. In this context, the entropy $H(x)$ of the variable x is utilized as a measure of its randomness. The Shannon entropy of a variable that can take random values represents a metric of its uncertainty before its value is unveiled [39]. This can be described as

$$H(x) = H(p_1, \ldots, p_N) = -\sum_n p_n \log_2(p_n), \tag{19}$$

where the coefficients p_n represent the probabilities of obtaining specific outcomes. By definition, Shannon entropy is

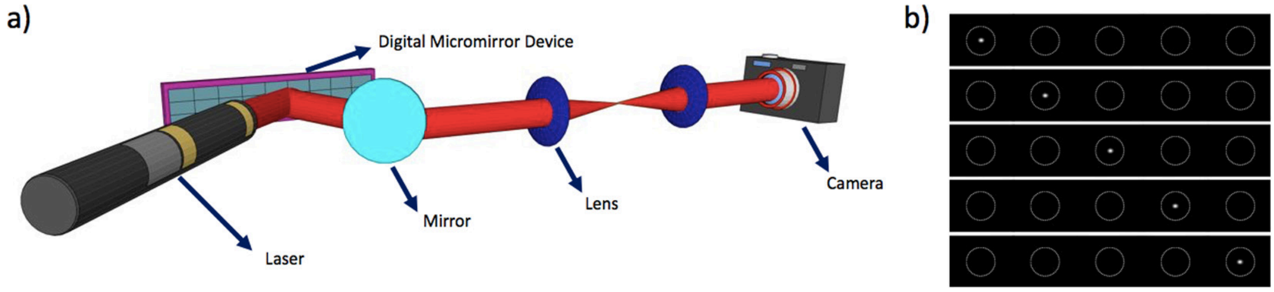

Figure 4. (a) A digital micromirror device (DMD) is utilized to prepare high-dimensional photonic states in the spatial degree of freedom. The pixels of the DMD direct light at the single-photon level to five spatial positions with equal probability. A sensitive camera is used to detect photons at different spatial locations, see (b).

expressed in units of bits. Ideally, the amount of information that can be encoded or decoded in the two dimensional states described in equations (13) and (14) can be quantified as follows

$$H(0.5, 0.5) = -0.5\log_2(0.5) - 0.5\log_2(0.5) = 1 \text{ bit}. \tag{20}$$

In this case, p_n equals to 0.5, this quantity results from the modulus squared of the amplitude coefficients in equations (13) and (14) that are equal to $1/\sqrt{2}$. According to this simple calculation, it is possible to use the polarization degree of freedom of a single photon to encode one bit of information. For this reason, quantum states with similar functional form as those in equations (13) and (14) receive the name of qubits. The amount of information that can be encoded in a photon described by a two dimensional state decreases as the random nature of the physical bit decreases. For example, the informational content of a two dimensional state decreases if one prepares a photon in the state $1/2|H\rangle + \sqrt{3}/2|V\rangle$. The value of Shannon entropy decreases for this polarization state

$$\begin{aligned} H(0.25, 0.75) &= -0.25\log_2(0.25) - 0.75\log_2(0.75) \\ &= 0.811 \text{ bit}. \end{aligned} \tag{21}$$

As discussed below, there are various mechanisms that can be employed to increase the information content of a single photon. For instance, instead of using its polarization properties, one can utilize additional properties of photons such as OAM or linear photon momentum [3]. In addition, multiple degrees of freedom of photons can be combined in a single communication protocol to increase the amount of information that can be imprinted in a photon [40]. The orthogonal bases in this family of communication protocols enable the implementation of high-dimensional Hilbert spaces [3, 41]. Interestingly, the transverse spatial degree of freedom has offered a flexible platform to test complex quantum information protocols in relatively simple fashions [8, 9, 30]. For example, quantum high-dimensional protocols have been implemented by defining Hilbert spaces in the pixel basis [8, 30, 35, 42]. These protocols have been demonstrated through the use of diffractive devices such as DMDs and SLMs.

Recently, there has been a strong impetus to employ discrete pixel basis in high-dimensional quantum protocols [8, 30, 35, 42, 43]. As discussed below, this photonic degree of freedom has been utilized in the context of quantum state engineering, quantum state tomography and information processing. For example, pixel entanglement was utilized to generate qudits [30], this idea was further extended by Dixon and co-workers who demonstrated information encoding in high-dimensional entangled states defined in the pixel basis [35]. In these cases, the Hilbert space is defined by the number of active pixels in spatial modulators of light, for example SLMs or DMDs [8, 30, 35, 42, 43]. In figure 4(a), we illustrate a simple scheme in which a diffractive device is utilized to randomly direct photons to one of five spatial positions. As shown in figure 4(b), one can use a sensitive camera with the capability of detecting single photons to decode information. In practice, the number of states in the Hilbert space is much smaller than the number of pixels in the DMD. Consequently, the five groups of pixels and the five possible spots detected by the camera define a high-dimensional system described by the superposition of five states [43]. In this case, the random diffraction of light from the five groups of pixels allows one to utilize Shannon entropy to study the potential of this communication protocol under ideal conditions. Given the fact that the probability of detecting a photon in each of the five locations is the same, the Shannon entropy can be calculated as

$$\begin{aligned} H(0.2, \ldots, 0.2) &= 5[-0.2\log_2(0.2)] \\ &= 2.32 \text{ bits}. \end{aligned} \tag{22}$$

This example shows that it is possible to increase the information content of a single photon by increasing the dimesionality of the state. Thus, it is possible to encode the same amount of information by preparing a five-dimensional state in other degrees of freedom, for example one can use the OAM of light [31, 41]. In practice, technology enables manipulation of specific properties of light, such as polarization. However, remarkable challenges in the manipulation of other properties of light have imposed important limitations in high-dimensional quantum information protocols. As discussed below, the possibility of using multiple degrees of freedom of multiple entangled photons represents a promising path to increase the informational capacity of high-dimensional photonic states [34, 35, 44]. Below, we describe how some of these ideas can be further extended to protect or compress information encoded in quantum photonic states.

3. Spatial correlations

In this section we introduce the underlying physics behind classical and quantum correlations of light. We start by describing the concepts of coherence and statistical fluctuations of light in the framework of optical physics [45]. This discussion is followed by a brief description of the Hanbury Brown and Twiss experiment [46]. The second part of this section introduces some of the fascinating aspects of quantum correlations in optical systems. Naturally, these ideas are presented in the context of the Einstein–Podolsky–Rosen effect [47, 48]. This effect is described in the variables of linear position and linear momentum, and ANG and OAM [49].

3.1. Coherence and fluctuations of light beams

The advent of the laser gave an enormous impulse to the development of the theory of optical coherence [45]. The fundamental statistical fluctuations of light that define the nature of correlations are described by this fundamental theory. In this section, we provide a brief review of the concept of spatial coherence, a property that will be used in several parts of this review.

The famous Young's double slit experiment has been widely used in different fields of physics [50–54]. Originally this setup was utilized to prove the wave nature of light [55]. However, this experiment can also be utilized to illustrate the concept of first-order coherence [45]. For this purpose, we use the setup depicted in figure 5. We assume that the slits are illuminated with a quasi monochromatic source of light with a beam waist located at $z = 0$. We also assume that the transverse profile of the source is partially coherent. The properties of first-order coherence can be quantified through the evaluation of the intensity measured by the detector located in the far-field of the two-slit arrangement at the transverse position x. The total electric field at the detector $E_d(x)$ is given by the sum of the instantaneous field amplitudes $E(x_1, z)$ and $E(x_2, z)$ transmitted through the slits. This can be expressed as

$$E_d(x) = a_1 E(x_1, z)\mathrm{e}^{\mathrm{i}k_0 d_1} + a_2 E(x_2, z)\mathrm{e}^{\mathrm{i}k_0 d_2}. \tag{23}$$

The magnitude of the wavevector in vacuum is represented by k_0 and the distances from the upper and lower slits to the detector D are represented by d_1 and d_2 respectively. The complex coefficients a_1 and a_2 represent the transmission amplitudes associated to the slits, the values for a_1 and a_2 are defined by the geometry of the slits. The intensity measured by the detector is given by the ensemble average of the instantaneous intensities given by the product $E_d^*(x)E_d(x)$. This quantity is defined as

$$\begin{aligned} I_d(x) &= \langle E_d^*(x)E_d(x)\rangle \\ &= |a_1|^2 I_1(x_1, z) + |a_2|^2 I_2(x_2, z) \\ &\quad + a_1^* a_2 \Gamma^{(1)}(x_1, x_2, z)\mathrm{e}^{-\mathrm{i}k_0(d_1-d_2)} + \text{c.c.}, \end{aligned} \tag{24}$$

where I_1 is defined as $\langle E^*(x_1, z)E(x_1, z)\rangle$ and I_2 as $\langle E^*(x_2, z)E(x_2, z)\rangle$, the ensemble average is denoted by $\langle \ldots \rangle$. The intensities I_1 and I_2 provide information about self-field correlations that can be described by the functions of first-order coherence $\Gamma^{(1)}(x_1, x_1, z)$ and $\Gamma^{(1)}(x_2, x_2, z)$. Similarly, the mutual-field correlation at plane z is described by the function of first-order coherence $\Gamma^{(1)}(x_1, x_2, z)$. The Gaussian Schell-model beams are a common example of a partially coherent beam [56]. Such a beam is defined by having a Gaussian intensity $I = \mathrm{e}^{-x^2/2\sigma_I^2}$, as well as a Gaussian first-order coherence $\Gamma^{(1)}(x_1, x_2, z) = \sqrt{I_1(x_1, z)I_2(x_2, z)}\mathrm{e}^{-|x_1-x_2|^2/2\sigma_\mu^2}\mathrm{e}^{-\mathrm{i}k_0(r_1-r_2)}$, where r_1 and r_2 are the distances from the center of the beam at the origin to slit 1 and 2, respectively. This beam can be used to define the intensity measured by the detector as

$$\begin{aligned} I_d(x) &= |a_1|^2 I_1(x_1, z) + |a_2|^2 I_2(x_2, z) \\ &\quad + 2|a_1||a_2|\sqrt{I_1(x_1, z)I_2(x_2, z)}\mathrm{e}^{-|\Delta x|^2/2\sigma_\mu^2}\cos(k_0\Delta s), \end{aligned} \tag{25}$$

where Δs is equal to $r_1 + d_1 - r_2 - d_2$. This result demonstrates that the formation of interference fringes occurs only when the length of the spatial coherence of the illuminating beam is larger than the separation of the two slits. In other words, interference fringes are formed when the properties of light are similar at the spatial locations defined by the two slits. This similarity is defined by the function of first-order coherence $\Gamma^{(1)}$. The concept of first-order coherence is also used to describe the similarity of light fields at different times, this property is known as temporal coherence [45].

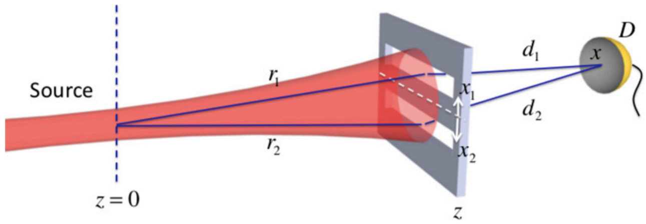

Figure 5. Schematic representation of the Young's double-slit interferometer used to illustrate first-order interference and first-order coherence. The quantities r_1 and r_2 represent the distances from the center of the source beam at plane $z = 0$ to the upper and lower slits, respectively. The two slits are separated by δx defined as $x_1 - x_2$, where x_1 represents the transverse position of the upper slit and x_2 represents the position of the lower slit. The distances from the upper and lower slits to the detector D are represented by d_1 and d_2 respectively.

3.2. Hanbury Brown and Twiss effect

In 1956, Hanbury Brown and Twiss (HBT) initiated the field of quantum optics with the observation of a novel form of interference produced by correlations of intensity fluctuations of light emitted from a chaotic source [45, 46]. Their stellar interferometer, designed to determine diameters of stars, consists of two detectors located at different positions on Earth that collect light produced by independent sources on the disc of a star [57]. The observation of an interference effect through the correlation of intensities was intriguing because at that time it appeared that classical and the primitive quantum theories of light offered different predictions.

The experimental setup depicted in figure 5 utilizes one detector at an specific location to infer coherence properties of a light beam that illuminates the two slits. Measurements

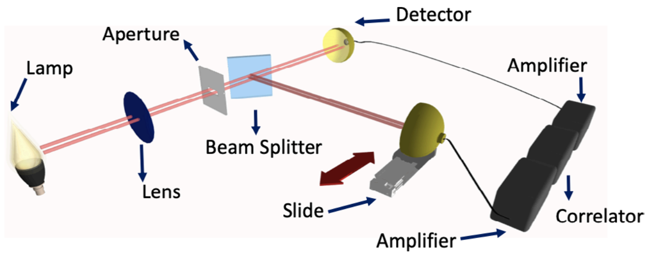

Figure 6. Schematic representation of the Hanbury Brown and Twiss interferometer. A mercury lamp is spatially filtered and measured by two detectors. One of the detectors is fixed whereas the second dectector is laterally displaced. The output signals of both detectors are correlated. This measurement is equivalent to the measurement of correlations of intensity fluctuations.

that utilize similar configurations enable the characterization of first-order coherence properties of the light beam. However, it is possible to study coherence properties of a source of light by performing measurements of intensity at two different spatial locations, see figure 6 . These measurements unveil properties of second-order coherence of the source. Interestingly, for coherent light emitted by a laser, this metric reveals that the statistical properties of the field at two spatial or temporal locations are independent and do not change in the spatial or temporal domain. In this case, the degree of second-order coherence for coherent light is equal to one. However, thermal sources of light are characterized by interesting properties of second-order coherence [58]. The generic function for second-order coherence is defined as

$$\Gamma^{(2)}(r_1, t_1, r_2, t_2) = \langle E^*(r_1, t_1)E(r_1, t_1)E^*(r_2, t_2)E(r_2, t_2)\rangle, \tag{26}$$

this function describes a statistical average of intensities associated to the fields $E(r_1, t_1)$ and $E(r_2, t_2)$. In general, the fields are detected at two different spatial and temporal positions.

As investigated by HBT, the experimental setup shown in figure 6 can be utilized to measure the second-order coherence function in equation (26). The HBT experiment consists of a source of pseudothermal light, in this case, a mercury lamp that is spatially filtered by a rectangular aperture and divided by a beam splitter. Then the two resulting beams are measured by two detectors located in the arms of the experiment. The position of one detector is fixed whereas the other detector is free to move in the transverse plane of the beam [46]. Given the finite size of the source, the two detectors can collect light from different spatial locations of the beam as shown in figure 6. The detected portions of the light beams are generated by a large number of independent emitters, these independent contributions to the detected field are described by $E_i(r_1, t_1)$ and $E_i(r_2, t_2)$, the subindex i represents the contributions from an emitter. Using this information, one can write the function of second-order coherence as

$$\begin{aligned}&\Gamma^{(2)}(r_1, t_1, r_2, t_2)\\ &= \left\langle \sum_{i,j,k,l} E_i^*(r_1, t_1)E_j(r_1, t_1)E_k^*(r_2, t_2)E_l(r_2, t_2)\right\rangle.\end{aligned} \tag{27}$$

After identifying the conditions under which superpositions of random phases from independent fields do not contribute to the function of second-order coherence, one can obtain the following general expression in terms of the first-order coherence functions $\Gamma^{(1)}$ [58]

$$\begin{aligned}&\Gamma^{(2)}(r_1, t_1, r_2, t_2)\\ &= \Gamma^{(1)}(r_1, t_1, r_1, t_1)\Gamma^{(1)}(r_2, t_2, r_2, t_2) + \left|\Gamma^{(1)}(r_1, t_1, r_2, t_2)\right|.\end{aligned} \tag{28}$$

In contrast to the separable second-order coherence function that characterizes coherent light, the coherence function for thermal light cannot be mathematically separated. As shown in equation (28), the thermal second-order coherence function can be written in terms of first-order coherence functions. As described in the previous section, first-order coherence functions quantify field correlations. Consequently, the first term in equation (28) describes a product of independent intensities. Furthermore, the second term $\left|\Gamma^{(1)}(r_1, t_1, r_2, t_2)\right|$ describes cross-field correlations. Interestingly, $\left|\Gamma^{(1)}(r_1, t_1, r_2, t_2)\right|$ cannot be mathematically separated through factorization. This implies that $\left|\Gamma^{(1)}(r_1, t_1, r_2, t_2)\right|$ cannot be written as the product of two fields at coordinates r_1, t_1 and r_2, t_2. This second term in equation (28), induces point-to-point correlations. In fact, an important consequence of the functional form of this second-order coherence function is the presence of intensity correlations in thermal beams of light [59]. As described below, this interesting property has been utilized to generate correlated photonic technologies in the classical domain.

3.3. Einstein–Podolsky–Rosen effect with photons entangled in momentum and position

In 1935, Einstein, Podolsky and Rosen (EPR) identified one of the most remarkable and surprising consequences of quantum physics, nonlocality [47]. This mysterious property of quantum systems was utilized as a solid argument to question the validity of quantum mechanics. In their influential paper, EPR analyzed a system of two distant particles entangled simultaneously in their position and momentum properties [47]. They pointed out that in a system with these properties one could perform a measurement of either position or momentum of one of the particles and infer, with complete certainty, either the position or momentum, respectively, of the unmeasured particle. In their emblematic gedanken experiment, the two distant particles do not interact and thus the possibility of inferring information of a distant particle would imply that the position and momentum of the unmeasured particle were simultaneous realities, leading to a violation of the Heisenberg's uncertainty principle. Remarkably, over the past 25 years, a series of systematical experimental tests have demonstrated that entanglement is in fact a real property of quantum mechanical entities such as molecules, atoms and photons [48, 49, 60].

A quantum state that ideally describes the EPR paradox can be described as follows

$$|\mathrm{EPR}\rangle = \int_{-\infty}^{\infty}\int_{-\infty}^{\infty} \delta(x_1 - x_2)|x_1, x_2\rangle \mathrm{d}x_1 \mathrm{d}x_2 \\ = \int_{-\infty}^{\infty}\int_{-\infty}^{\infty} \delta(k_1 + k_2)|k_1, k_2\rangle \mathrm{d}k_1 \mathrm{d}k_2. \tag{29}$$

The product states $|x_1, x_2\rangle$ and $|k_1, k_2\rangle$ represent the position and momentum bases of the particles, respectively. The states in equation (29) describe entanglement in the position and linear momentum basis [48]. In this case, the nonseparable function $\delta(x_1 - x_2)$ describes perfect punctual position correlations in the biphoton system, similarly $\delta(k_1 + k_2)$ describes perfect anti-correlations in the space of linear momentum. This means that if a photon in a EPR state is detected at position x', the second photon in the pair will be found at the same position x'. Similarly, if a photon in the pair is detected in the spatial frequency k', the spatial frequency of the second photon will be $-k'$. In this case, the photons are anti-correlated in the variable of linear momentum. In contrast to the second-order correlation function that describes thermal radiation, the EPR states are only characterized by nonseparable functions that lead to strong point-to-point correlations [59]. These two mechanisms can be discriminated by measuring the variances in the measurement of position and momentum correlations. In general, photons in thermal states satisfy the following inequality

$$(\Delta x_2|_{x1})^2(\Delta k_2|_{k1})^2 < \frac{1}{4}, \tag{30}$$

in contrast, photons in quantum mechanical EPR states violate the inequality. In this case, $\Delta x_2|_{x1}$ denotes the uncertainty in the measurement of the position of one photon x_2 conditioned upon measurement of the other photon in x_1, a similar situation holds for $\Delta k_2|_{k1}$. The inequality in equation (30) bounds the strength of spatial correlations for beams of light that can be described by the classical theory of coherence, for example thermal and coherent light beams [45, 46]. The bounds in this inequality result from the spatial variances in the position and momentum space as predicted by the diffraction theory of light [47, 48]. For instance, one might employ a narrow slit to perform an accurate measurement of the spatial position of photons emitted by a source. However, the presence of the narrow slit will produce diffraction that will make extremely hard to measure the momentum of photons with small uncertainties. Notably, the violation of this inequality, via correlation measurements, indicates the presence of optical fields characterized by nonclassical correlations such as EPR beams [47, 48]. As described below, a quantum system with these characteristics offers new possibilities for encoding multiple bits of information and for performing imaging with unique features [1, 2, 61].

Interestingly, the process of SPDC offers the possibility of generating pairs of entangled photons with characteristics that strongly resemble those described in the EPR paradox [48, 49, 62]. As depicted in figure 7, SPDC is a nonlinear process in which one pump photon is annihilated to generate entangled photon pairs [63]. As described in figures 7(b) and (c), linear momentum and energy are conserved in this nonlinear process. The nature of the correlations in the spatial degree of freedom is illustrated in figure 7(a), in this case, a pair of entangled photons is generated at the same crystal position and consequently the photons are correlated in the variable of linear position. As shown in figures 7(a) and (b), the conservation of linear momentum forces the two beams to propagate with opposite spatial frequencies [63]. Thus, SPDC photons are characterized by opposite transverse wavevectors that induce anti-correlations in linear momentum.

3.4. Einstein–Podolsky–Rosen effect with photons entangled in OAM and ANG

It is convenient to devote part of this section to discuss the Fourier relationship existing between the ANG and OAM variables of an optical beam [64]. These physical variables are utilized to illustrate the EPR paradox in the azimuthal degree of freedom. Similarly to linear position and linear momentum, ANG and OAM are conjugate variables and they form a Fourier pair [65]. The Fourier relations are expressed as follows

$$\Psi(\ell) = \frac{1}{\sqrt{2\pi}}\int_{-\pi}^{\pi} \mathrm{d}\phi\psi(\phi)\exp(-\mathrm{i}\ell\phi); \\ \psi(\phi) = \frac{1}{\sqrt{2\pi}}\sum_{-\pi}^{\pi} \Psi(\ell)\exp(\mathrm{i}\ell\phi). \tag{31}$$

Here $\Psi(\ell)$ represents the probability amplitude that a photon is carrying the OAM number ℓ, whereas $\psi(\phi)$ is the probability amplitude that the ANG of the photon is ϕ. From these relations, it is important to note that a rotation $\Delta\phi$ will induce a phase that is ℓ-dependent and is given by $\Delta\phi\ell$ [64]. Below we discuss the relevance of this parameter for the estimation of angular rotations.

The Fourier relations described by equation (31) can be illustrated with the cartoon shown in figure 8. It is shown that a beam with a uniform spatial profile does not carry OAM and consequently the OAM spectrum is centered at zero. In contrast, a beam shaped in a form of angular wedge shows a broader OAM spectrum. The spectrum is broad for angular modes with narrow widths and narrow for broad angular modes. This behavior is a manifestation of the uncertainty principle for the azimuthal variables of ANG and OAM.

The multiple degrees of freedom of light have been exploited to perform multiple tests of quantum mechanics under specific conditions. In 2010, Leach and colleagues demonstrated EPR correlations in the basis of ANG and OAM [49]. This demonstration utilized the conservation of OAM in SPDC processes. In this case, a pump beam with a Gaussian spatial profile ($\ell = 0$) produces down-converted photons with opposite OAM numbers. In this case, the width of the spiral spectrum of the down-converted photons depends on the phase matching conditions of the SPDC process.

The experimental setup depicted in figure 9 was utilized by Leach *et al* to implement the EPR paradox in the azimuthal basis [49]. In this case, a BBO crystal was pumped to generate photon pairs with opposite OAM values. The down-converted photons are separated by a beam splitter and then projected onto SLMs [27]. A series of computer generated holograms,

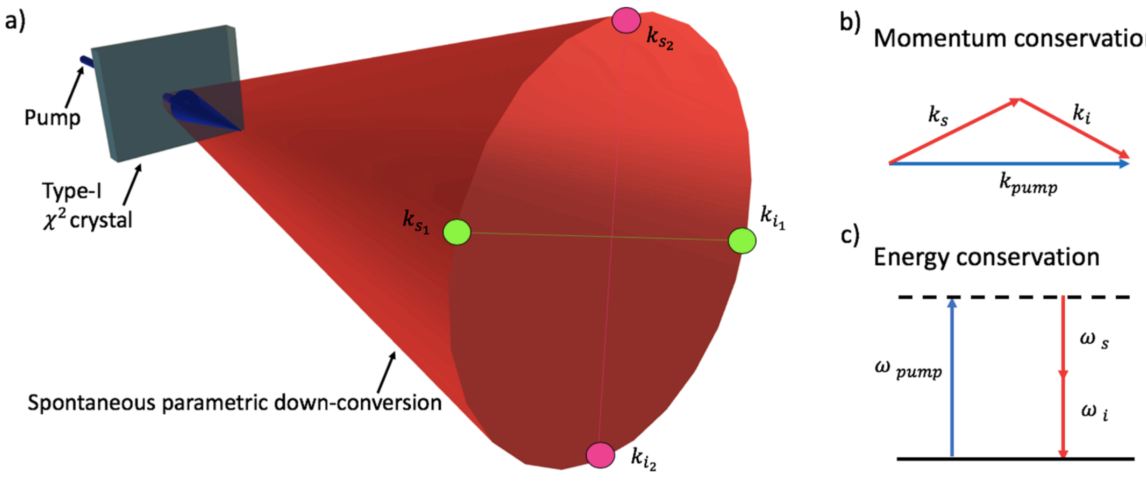

Figure 7. (a) The process of spontaneous parametric down-conversion (SPDC) is produced by pumping a $\chi^{(2)}$ nonlinear crystal. The SPDC photons are generated at the same spatial position in the crystal and consequently photon pairs are correlated in the variable of spatial position. The conservation of linear momentum shown in (b) forces a pair of SPDC photons to be anti-correlated in the variable of linear momentum. Consequently, photons located in opposite positions of the down-conversion cone are correlated. As shown in (c), the process of SPDC satisfies conservation of energy, in this case, a blue photon is annihilated to create two red photons.

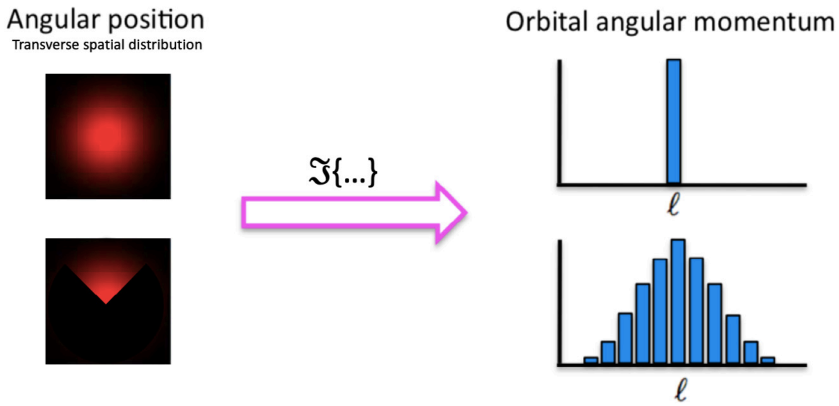

Figure 8. Fourier relationship between ANG and OAM. A broad OAM spectrum is observed for an angular mode with narrow width. This is a manifestation of the uncertainty principle for the conjugate variables of ANG and OAM.

displayed on the SLMs, were utilized to measure the ANG and OAM of signal and idler photons. The ANG was determined by displaying angular sectors with different rotations whereas the OAM spectrum was measured by using forked diffraction gratings. As shown in figures 9(b) and (c), the down-converted photons are strongly correlated in the variable of ANG and anti-correlated in their OAM numbers. The strength of the correlations is quantified through the use of an inequality that shares similarities with that shown in equation (30). Remarkably, the team reported a strong violation of the inequality that demonstrated the nonclassical nature of the detected correlations [49]. The identification of these azimuthal correlations has serious consequences for the fields of quantum information science and quantum imaging, some of the next sections are devoted to discuss implications of azimuthal EPR correlations.

4. Quantum imaging

The identification of the quantum properties that characterize beams of light has led to novel schemes for correlated imaging [66–74]. It results remarkable the fact that classical correlated imaging was triggered by experimental demonstrations of quantum spatial correlations and not by the HBT effect [68]. We start this section by reviewing classical imaging techniques that rely on intensity correlations. Then, we devote the rest of the section to describe the quantum features that make quantum imaging an important quantum technology [75].

4.1. Classical coincidence imaging

In contrast to other quantum photonic technologies in which the quantum properties of light are utilized to boost the performance of a classical protocol, classical schemes for coincidence imaging were developed in parallel to their quantum counterparts. This field initiated in 2002 when Bennink, Bentley and Boyd demonstrated the possibility of performing coincidence imaging without entanglement [68]. In general, this technique utilizes correlations between two beams of light to form an image. More specifically, in this protocol one of the correlated beams illuminates a known reference system, while the other travels through an unknown test system. The location

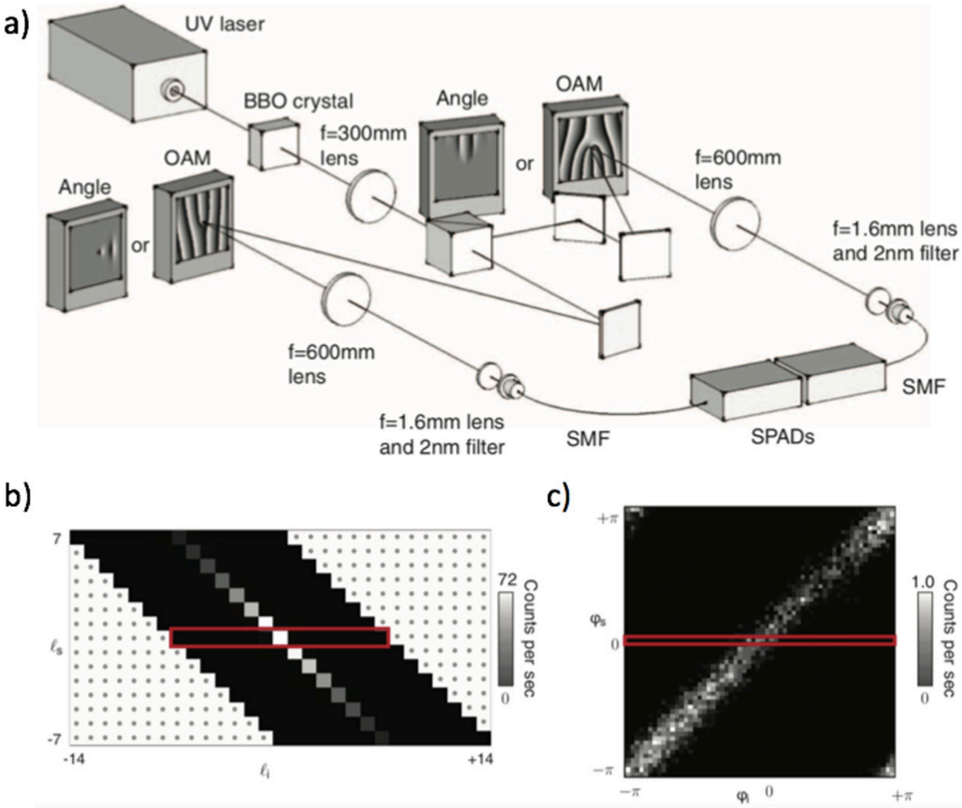

Figure 9. (a) The conservation of momentum in SPDC processes generates photon pairs correlated in the variable of ANG and anti-correlated in the variable of OAM. These correlations give rise to the azimuthal version of the EPR paradox. These properties are measured by means of two SLMs and single mode fibers. The experimental verification of OAM anti-correlations is shown in (b), the measurements that demonstrate the presence of angle correlations are shown in (c). Reprinted with permission from [49].

of the reference photon is recorded on a detector array, while a second detector, known as bucket detector, registers the events in which the test photon has been detected. Remarkably, an image of the unknown object appears on the spatially resolving detector via correlations, even though the photons in the reference system never interacted with the object.

In their seminal paper, Bennink and co-workers utilized a probabilistic approach to identify the conditions under which classical sources of light can mimic the functionality of entangled sources for imaging purposes [68]. Interestingly, the team demonstrated that this is possible when the function of second-order coherence is described by a nonseparable function. As discussed above, either pseudothermal sources of light and biphoton states are characterized by correlation functions that are not separable, see equations (28) and (29). Furthermore, the team performed the experiment depicted in figure 10(a). This experimental setup utilizes a classical source of light (HeNe laser), an optical chopper and a movable mirror to produce angularly correlated pulses that are splitted and sent to the reference and test arms. As shown in figure 10(a), one of the pulses illuminates an object and is then collected by a bucket detector, which does not provide spatial information. Its correlated pulse is detected by a camera that is gated by the first photon's bucket detector. Interestingly, no pattern is observed by averaging all frames when the camera is not gated, however, a pattern is formed by averaging the gated frames, an example of the pattern formed in correlations is shown in figure 10(b).

This classical scheme for correlated imaging has motivated various research lines in the last two decades [69–75]. An important example is the development of novel families of cameras that we review in the next section. In addition, novel proposals that utilize natural sources of light to implement light detection and ranging (LiDAR) are subject of active research [71, 72, 74, 76]. Last but not least, the use of classical intensity correlations has been exploited to encrypt information in the spatial profile of light beams [77, 78].

4.2. Quantum coincidence imaging

The nonlocal characteristics of EPR states stimulated multiple protocols for quantum information science [1, 2]. In the field of imaging, entangled photons in the variables of position and momentum have been utilized to demonstrate the formation of quantum images with unique signal-to-noise levels and resolution features [75]. The first scheme for quantum imaging was demonstrated in 1995 by Pittman and co-workers [66]. Due to the surprising nonlocal features of the first quantum imaging protocol, this received the name of 'ghost imaging' [67]. The setup utilized in the demonstration of ghost imaging is depicted in figure 11. This consists of a laser beam that is used to pump a nonlinear crystal to produce correlated photon

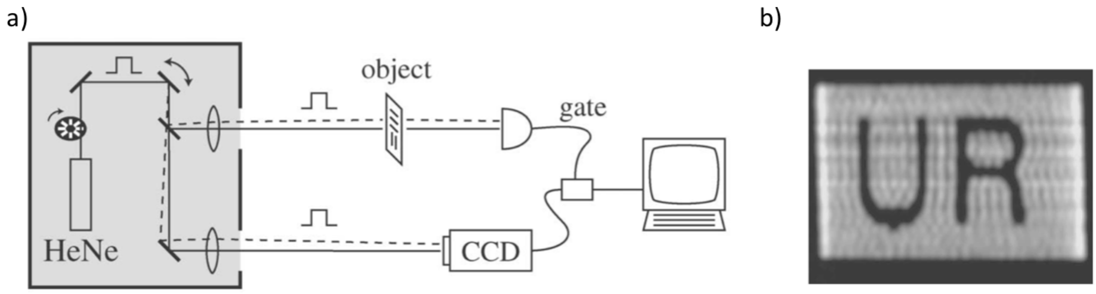

Figure 10. (a) The experimental setup used to demonstrate coincidence imaging with a classically correlated source. (b) The image formed in the reference arm when the camera is gated by the detector in the test arm. Reprinted with permission from [68].

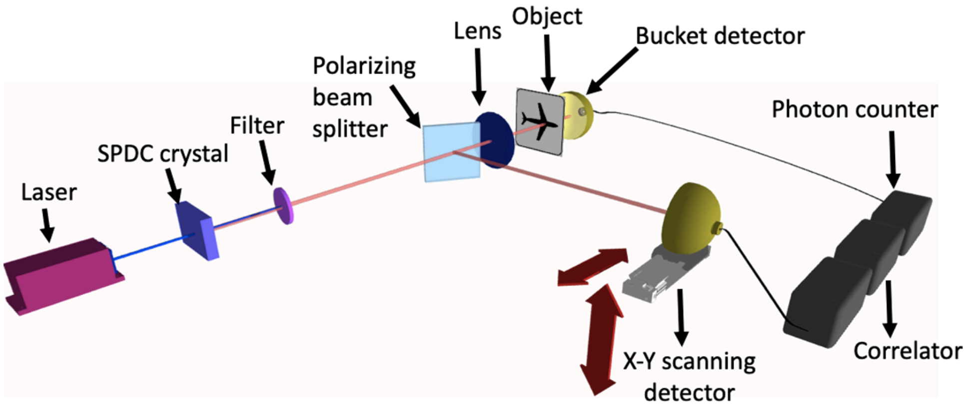

Figure 11. (a) The experimental setup used to demonstrate coincidence imaging with a quantum correlated source. The image is formed through the correlations between the bucket detector and the detector used for raster scan measurements.

pairs with orthogonal polarization. Signal and idler photons are separated by a polarizing beam splitter (PBS). The signal photon passes through a lens, an object and is finally measured by a bucket detector. The idler photon is measured by a detector that is mounted on a raster scan system to provide spatial resolution. The output signal from each detector is processed by a coincidence circuit that is used to count joint photon-detection events. Interestingly, the image of the object is only formed in coincidences. Furthermore, the magnification of the object is determined by the ratio between the distance from the lens to the object s_0 and the total distance s_i from the lens to the crystal and from the crystal to the raster scan system. Interestingly, the imaging conditions for this quantum correlated scheme is described by the well-known thin lens formula $1/f = 1/s_o + 1/s_i$.

The possibility of using the simple thin lens formula to describe quantum coincidence imaging allows the unfolding of the experimental setup for ghost imaging. As shown in figure 12, this is possible because the ray diagram for the corresponding imaging system reproduces correlations in the plane of the crystal and anti-correlations in the Fourier plane of the imaging system. In this case, the rays that represent the signal and idler photons can be traced back to the same position in the crystal, this implies that both photons are generated at the same transverse position in the crystal, see green arrows in figure 12. Furthermore, the rays for signal and idler modes can be extended to the Fourier plane of the imaging system. As discussed above, the Fourier plane in this configuration corresponds to the transverse momentum space of the imaging system. In this case, the transverse component of the photons have opposite directions, thus signal and idler show anti-correlations in the variable of momentum.

4.3. Sub-shot-noise imaging

Besides the nonlocal properties discussed above, photon pairs generated by the process of SPDC show other nonclassical properties that have been utilized to form images with unique spatial features [5, 79, 80, 81]. In this section, we describe the noise properties that can be achieved by manipulating quantum states of light. More specifically, we review the experimental demonstration of sub-shot-noise quantum imaging [80, 81]. This quantum imaging technique enables new possibilities to identify sensitive biological materials at low-light levels.

The quantum fluctuations that characterize different kinds of light induce different noise properties that can be utilized for the development of multiple quantum photonic technologies for metrology, communication, imaging and remote sensing [72–75, 80–83]. Coherent and thermal light beams are described by quantum mechanical states with classical noise properties, the photon number distributions of these beams are Poissonian and super-Poissonian, respectively [58]. In contrast, the nonclassical sub-Poissonian photon statistics of light beams produced through SPDC processes enable the formation of high-contrast images with unique spatial resolutions and signal-to-noise properties [79, 84]. Nevertheless, given the commonly low-conversion efficiencies of SPDC processes, these schemes for quantum imaging work at low-light

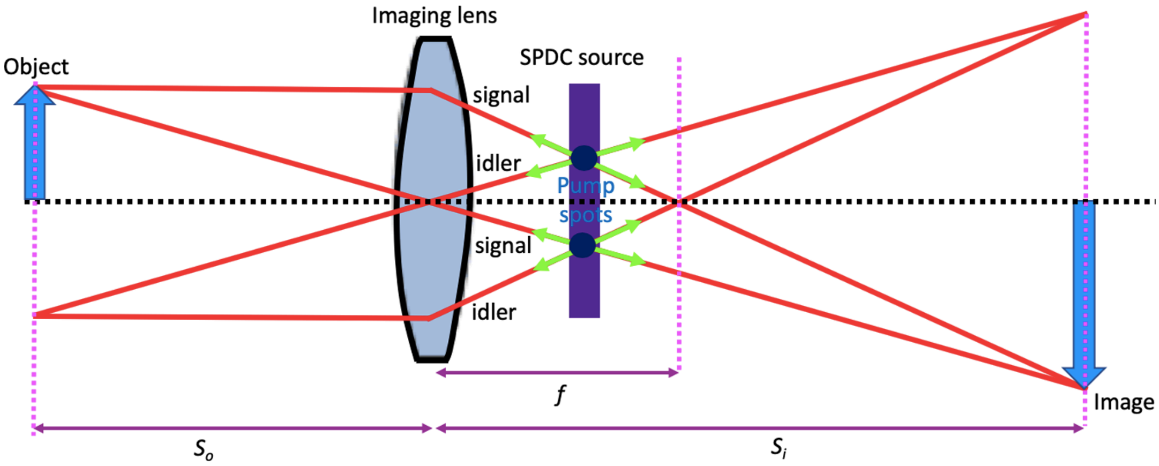

Figure 12. The unfolded ghost imaging diagram obeys the thin lens equation. The ray description of the imaging system reproduces transverse spatial correlations in the plane of the SPDC crystal. In addition, the transverse components of the signal and idler rays in the Fourier plane of the imaging system have opposite directions. This condition reproduces the expected anti-correlations in the variable of momentum. For sake of clarity, we illustrate two pump spots, however, these do not play a relevant role in the unfolded ghost imaging diagram. Furthermore, signal and idler beams are conjugate modes that can be arbitrarily labeled. Nevertheless, this notation should be used in a consistent fashion.

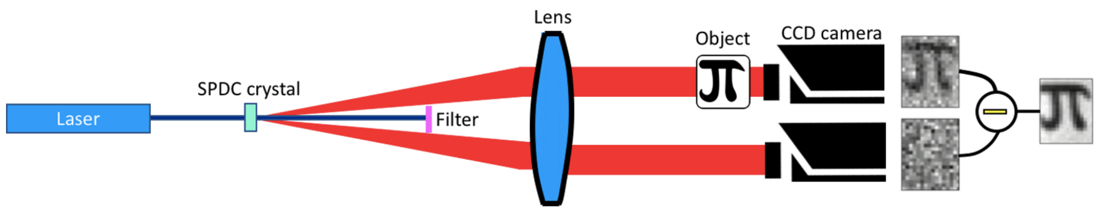

Figure 13. Experimental apparatus for differential quantum imaging. In this scheme, SPDC photons are used to image an arbitrary object, noise of the formed image is significantly reduced by performing differential measurements of the signal and idler fields.

levels. This feature has been exploited to perform imaging of materials that are sensitive to high levels of light.

In 2010, Brida and co-workers demonstrated a clean imaging protocol that enables one to form images with contrasts and noise properties that can only be achieved through quantum resources [81]. In the setup shown in figure 13, laser pulses are used to pump a nonlinear $\chi^{(2)}$ material that produces quantum correlated photon pairs. Signal and idler photons pass through a collimating lens, then, one of the down-conversion modes illuminates an object, the transmitted photons in this mode are detected by a CCD camera. Similarly, photons in the second mode are detected by the same CCD array. The protocol is formalized by subtracting correlated pixels in the CCD array. Due to the strong correlations between signal and idler modes, this operation leads to an improvement in the contrast and consequently to the significant reduction of noise in the retrieved image [81].

Two experimental realizations of differential quantum imaging are presented in figure 14(a). For sake of comparison, the classical implementations of differential imaging for same mean photon numbers are shown in figure 14(b). It is evident for this case that the contrast and noise in the images make the identification of the object extremely difficult. Finally, a direct classical imaging of the object is shown in figure 14(c). The latter implementation does not utilize differential measurements. Figure 14 demonstrates the potential and the advantages of differential quantum imaging. Interestingly, the reduction in the amount of noise in the protocol for quantum differential imaging cannot be explained using the classical theory of electromagnetic radiation. In other words, it is not possible to reproduce the signal-to-noise ratio in figure 14(a) using coherent or thermal states of light.

4.4. Fundamental limits on optical resolution

Now we turn our attention to the use of quantum correlations for surpassing classical resolution limits in optics. The interest in this sub-field of imaging was partially motivated by the possibility of fabricating denser patterns for integrated circuits and CMOS technology [5]. In 2000, Boto and co-workers proposed the possibility of beating the diffraction limit by exploiting entanglement [5]. This work was followed by D'Angelo *et al* who demonstrated the experimental observation of high-resolution fringes produced by two-photon interference, this effect is known as quantum superresolution [80]. The improved spatial resolution obtained through the use of certain quantum states of light can be understood as resulting from a combination of two effects. (1) A two-photon state of light has a de Broglie wavelength that is half that of the optical wavelength of each photon [85]. This decreased de Broglie wavelength can for certain geometries lead to an improved spatial resolution. (2) Squeezed states of light can be used to achieve a better signal-to noise ratio of optical measurements, which allows one to localize the position of a light beam to better than the standard

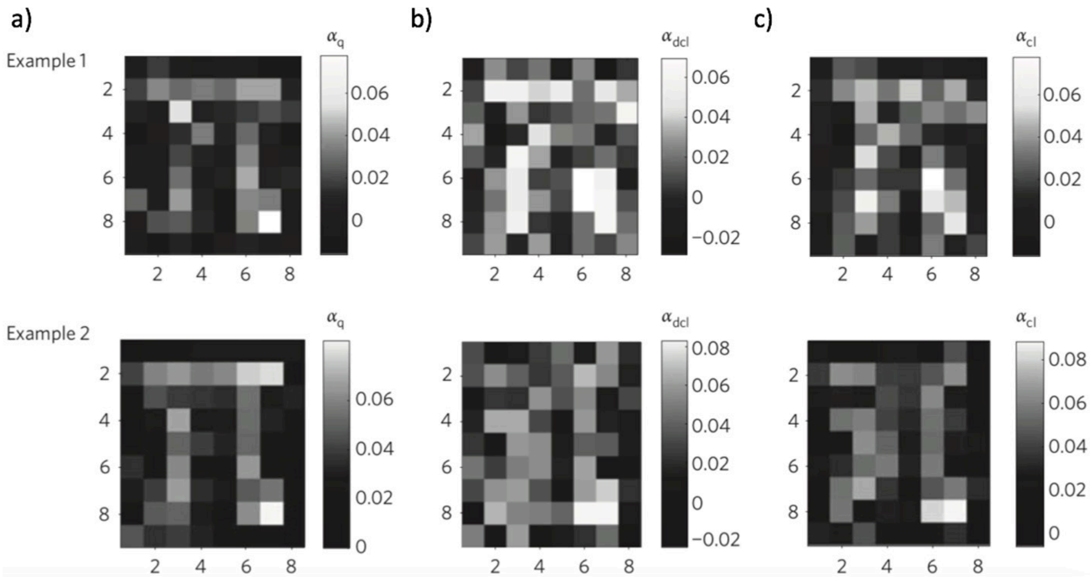

Figure 14. Experimental results for differential and conventional imaging. The mean numbers of photons per pixel is approximately 7000 for the three experiments. Two realizations of the differential imaging protocol with SPDC photons are shown in (a). The experimental results obtained with classical light sources are shown in (b). Images formed through conventional imaging (no differential measurements) are plotted in (c). Reprinted with permission from [81].

shot-noise limit [80]. These findings motivated almost two decades of active research in this field [2, 4, 6, 86, 87]. In the past few years, scientists have identified the quantum and classical features of optical superresolution [73, 88].

Nonclassical effects attributed to two-photon interference had already been observed in the eighties in the context of quantum fluctuations of light and quantum nonlocality [79, 89]. However, the spatial implications of two-photon interference and their importance for overcoming undesirable effects caused by diffraction started with the two-photon version of the Young's double-slit experiment [80]. In interferometry and imaging, wave diffraction establishes fundamental resolution limits that define the minimal resolvable feature size for an object, given a wavelength λ [45]. The Abbe–Rayleigh criterion represents one of the most common definitions for diffraction-limited resolution [5]. This stipulates that an optical system cannot resolve spatial changes smaller than $\lambda/2$. Remarkably, it has been demonstrated multiple times that this fundamental limit can be surpassed by exploiting quantum interference [6].

The experimental apparatus used to beat the diffraction limit through the two-photon Young's double slit experiment is depicted in figure 15. Here, photon pairs generated by the process of SPDC are passed through a double-slit arrangement. A PBS separates the generated down-converted photons with perpendicular polarizations. Signal and idler photons are measured by two single-photon detectors and the electronic signals produced by the detectors are then correlated. As shown in figure 16(a), an interference pattern is observed in coincidences, surprisingly no fringes are observed in singles. Furthermore, the frequency of the interference pattern is twice the frequency expected for the classical realization of the double-slit experiment [80]. This interesting feature measured by D' Angelo *et al* is shown in figure 16(b). It is important to point out that similar effects were then observed using classical intensity correlations in thermal light. In contrast to interference fringes produced by quantum interference effects, these classical interference structures are characterized by low visibilities due to the lack of perfect correlations in thermal beams of light [73, 88].

4.5. Quantum-secured imaging and optical encryption

The strong correlations of entangled photon pairs have motivated scientists and engineers to implement nonlocal operations to hide information [31, 76, 78]. Naturally, some of these protocols have been specifically designed to offer security in the transmission of information. In this section we review quantum-secure imaging and optical encryption [76, 78].

The protocol for quantum-secured imaging utilizes time-of-flight information of photons entangled in the polarization degree of freedom to image a remote object [76]. This protocol is capable of avoiding jamming in schemes for remote sensing such as LiDAR. More specifically, this protocol delivers to the user a secure image against attacks in which the object being imaged intercepts and resends photons with spoiled information. Any attempt to steal information disturbs the fragile quantum state of the imaging photons, this process introduces statistical errors that reveal its activity. The image is secure if entanglement between photons is preserved. In this case, the preservation of entanglement is quantified through a specific form of Bell inequality known as the Clauser, Horne, Shimony and Holt (CHSH) inequality [60]. This inequality utilizes the CHSH parameter $|S|$ to certify the presence of entanglement.

The protocol for quantum-secured imaging is illustrated in figure 17. This protocol is based on the Ekert protocol that uses polarization entanglement for security [90]. In this proof-of-principle experiment, a pulsed laser pumps a pair of crossed periodically-poled potassium titanyl phosphate (PPKTP) crystals to create polarization-entangled photons in the state $(|H_1H_2\rangle + |V_1V_2\rangle)/\sqrt{2}$ [62]. Using Pockels cell

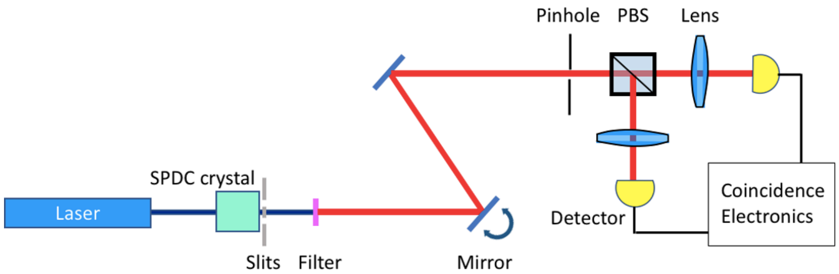

Figure 15. Experimental apparatus used to demonstrate two-photon interference in a Young's double slit experiment.

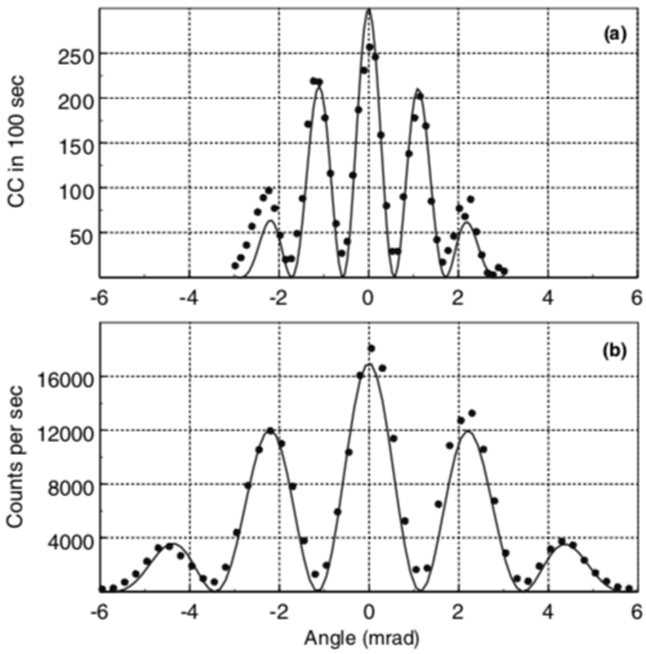

Figure 16. The Young's double-slit experiment performed with quantum and classical light. The interference structure produced by two-photon interference effects is shown in (a), the classical version of the experiment produces interference fringes with half the frequency measured for the quantum implementation, see (b). Reprinted with permission from [80].

(PC), a PBS, and two avalanche photodiodes (APDs) that are used as single-photon detectors, photon pairs are measured in the rotated polarization basis $|H'\rangle + |V'\rangle$, where $|H'\rangle = \sin\theta|V\rangle + \cos\theta|H\rangle$ and $|V'\rangle = \cos\theta|V\rangle - \sin\theta|H\rangle$. One photon from the polarization-entangled pair is measured by PC_a, PBS_a, APD_1, and APD_2 in one of two rotated polarization bases with $\theta = 0°$ and 45°. The other photon travels to the object and is reflected back to the source, where it is measured by PC_b, PBS_b, APD_3, and APD_4 in one of two rotated polarization bases with $\theta = 22.5°$ and $-22.5°$. For each pulse, coincidence timing measurements between $APDs_{1,2}$ and $APDs_{3,4}$ are used to calculate the CHSH parameter S [91], as well as the distance to, or velocity of the object [71]. If the estimated CHSH parameter satisfies the inequeality $|S| > 2$, the optical ranging measurement is secure against an intercept-resend jamming attack. This technique represents an alternative to enhance the security of current systems for optical ranging [71].

The active research performed in the field of optical encryption aims to develop effective methods to hide information encoded in multiple degrees of freedom of light [77, 78]. This can be achieved through different random phase-encoding schemes [77]. One important optical encryption scheme, known as double random phase encoding is depicted in figure 18(a). In this technique an image is multiplied by a random phase $\phi(x, y)$, then a Fourier transform is implemented by a lens. In addition, a second projection is implemented in the space of spatial frequencies, the protocol is formalized by performing an inverse Fourier transform. This protocol can also be implemented using a single phase screen [78]. In the past few years, there has been an important interest in performing optical encryption in quantum correlated imaging [75]. Here we review optical encryption based on ghost imaging.

The proposal of computational ghost imaging (CGI) served as a powerful platform for implementing a variety of novel protocols for quantum and classical imaging [92, 93]. In contrast to the conventional scheme for ghost imaging [66, 67], CGI allows one to use a single bucket detector and a raster scanning system to form images of arbitrary objects [92, 93]. This scheme was exploited by Clemente and colleagues to implement image encryption [78]. In their protocol, the team assumes that Alice wants to send an encrypted image to Bob. It is also assumed that Alice and Bob share a secret key that consists of a vector with multiple elements. Furthermore, Alice encrypts the image by using an arbitrary phase-only mask. This procedure produces a structured beam that is used to illuminate an object, the transmitted light is collected by a single-pixel detector. This operation is performed multiple times for different phase profiles. Thus, information about the object is encoded in a vector with multiple components that contains the corresponding intensity values detected by the single-pixel detector. These values are shared with Bob using a public channel, who uses this information to decrypt the image.

The image of an arbitrary object $\mathcal{O}(x, y)$ is recovered through the following linear operation

$$\mathcal{O}(x, y) = \frac{1}{N}\sum_{i=1}^{N}[B_i - \langle B\rangle]I_i(x, y), \tag{32}$$

where $I_i(x, y)$ denotes the intensity distribution that would be achieved in the reference arm, and $\langle B\rangle$ is the average value for the measured intensity values B_i. An important point to note in the use of CGI for optical decrytion is that the intensity patterns $I_i(x, y)$ can be easily computed by Bob according to equation (32), provided that the set of phase profiles is known.

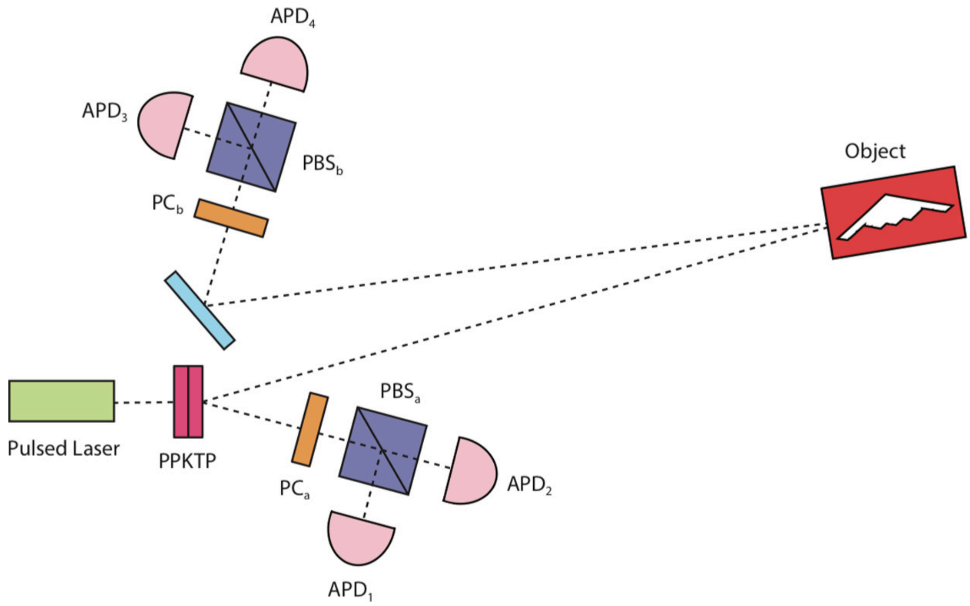

Figure 17. Schematic for a secure time-of-flight experiment, based on the Ekert QKD protocol. Polarization-entangled photon pairs generated through SPDC are used to measure the distance to an object. Security against an intercept-resend jamming attack is verified through a CHSH Bell test. Reprinted with permission from [76].

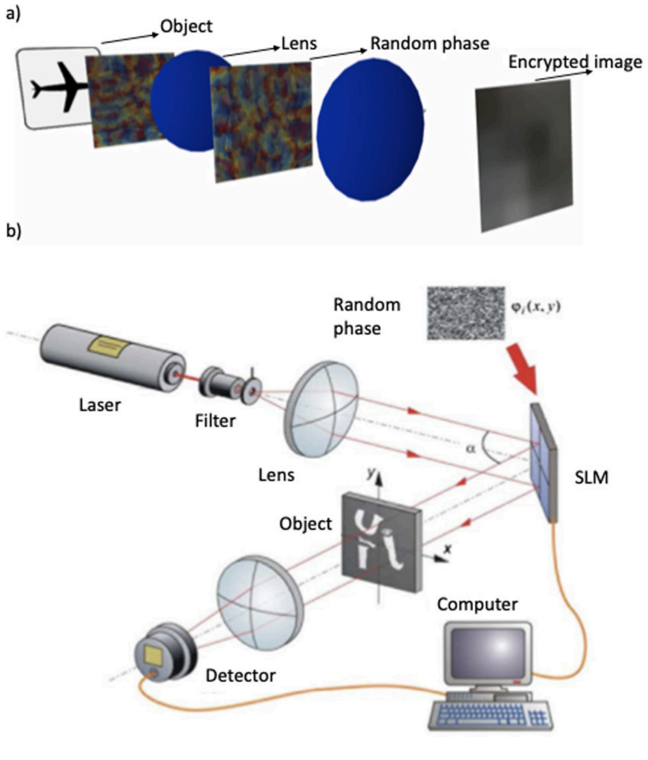

Figure 18. A typical setup for image encryption via double random phase encoding is shown in (a). Encryption of an object by means of double random phase encoding in a computational ghost imaging (CGI) protocol is depicted in (b). Reprinted with permission from [78].

5. CS for imaging

CS techniques exploit the potential of optimization algorithms to infer sparse signals from partial or incomplete sets of measurements [94, 95]. CS has been applied in multiple research fields ranging from seismology and medical science to quantum information science [95]. The mathematical formalism behind the optimization methods for CS are not discussed in this review. Instead, we focus our attention to illustrate the circumstances under which CS algorithms boost the performance of protocols for quantum imaging and information.

The typical experimental setup for CS in classical imaging is shown in figure 19. Here an object, represented by the vector O, is imaged onto a DMD where a series of random binary matrices are displayed, each matrix constitute a row in the total sensing matrix A. The reflected light from the DMD is collected by a focusing lens and measured by a photodiode, each measurement defines an element in the vector Y. In general, this imaging system can be described in the form $Y = AO$. It is possible to implement the complete matrix A to measure the total elements in Y; subsequently, this information can be used to invert the linear equation and determine the target object O. However, CS takes advantage of the sparsity in the target object by using optimization. This allows the estimation of the object O with only a small fraction of measurements. An approximation of the object O is obtained by solving the following optimization problem

$$\min_{O'} \|\nabla O'\|_{\ell_1} + \frac{\mu}{2}\|Y - AO'\|^2_{\ell_2}. \tag{33}$$

Here, $\nabla O'$ is the discrete gradient of O' with respect to pixel position, and μ is a regularization term. The optimal value of μ should be chosen considering the specific characteristics of the object O and the amount of noise in the data. The solution of the optimization problem in equation (33), through CS, allows one to estimate the object O' that is an approximation of the initial object O.

This imaging protocol has motivated the construction of single-pixel cameras [86], these are apparatus that use detectors with no spatial resolution to form images. In the classical domain, this technique represents an important alternative to

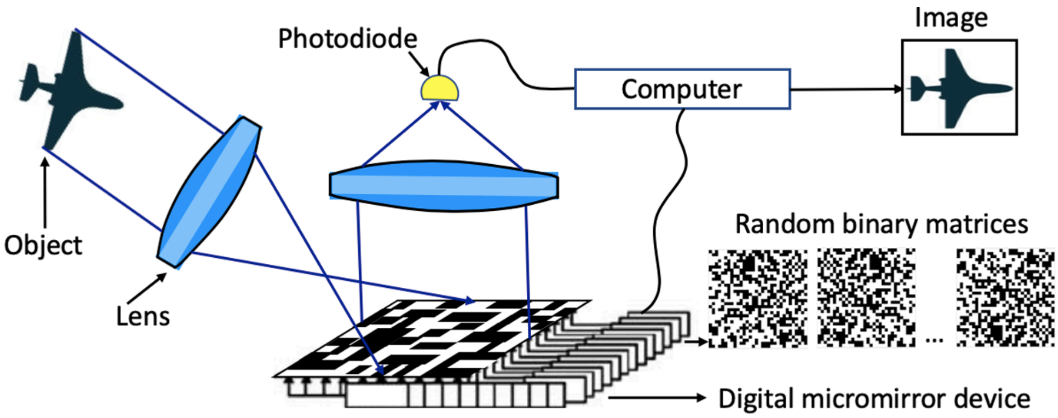

Figure 19. Experimental implementation of a single-pixel camera based on CS. Here, an arbitrary object is imaged by performing a series of random spatial projections on a DMD. Light reflected from the DMD is measured by a photodiode. The use of optimization allows the reconstruction of an image of the object with a small fraction of measurements with respect to conventional raster scan techniques.

perform imaging at long wavelengths where cameras are not available. In addition, the significant reduction in the number of measurements required to reconstruct an image represents another important characteristic that has made CS an attractive tool for applications in which the complete set of data is not available [96]. In the following sections, we describe three protocols for imaging that exploit sparsity and optimization.

5.1. Compressive imaging with entangled photons

The first implementation of a CS algorithm for quantum imaging was demonstrated by Zerom *et al* in 2011 [70]. In general, the process of SPDC is not efficient and consequently the photon flux of the down-converted photons is typically small [97]. Consequently, most techniques for quantum imaging require long integration times to form images with signal-to-noise ratios that allow their practical identification [98]. This problem is to some extent magnified by the raster scanning process employed in a significant number of schemes for single-photon imaging. As demonstrated by Zerom and co-workers, optimization algorithms for CS show potential to alleviate these problems that are ubiquitous in single-photon technologies [70].

The schematic that depicts the experimental arrangement for compressive imaging utilized by Zerom and colleagues is shown in figure 20(a). In this case, a nonlinear BBO crystal is pumped to produce entangled photon pairs. A lens is utilized to image the signal mode onto an object and the idler mode onto a SLM where CS is implemented. Signal and idler modes are measured by single photon detectors that lack of spatial resolution. The protocol is finalized by performing a series of correlations between signal and idler modes for the multiple random patterns displayed on the SLM. Mathematically, this can be expressed by means of the correlation function C_m as

$$C_m = \int \mathrm{d}x_1 \mathrm{d}x_2 \left| \langle \psi | \hat{E}^{(+)}(x_1) \hat{E}^{(+)}(x_2) | \psi \rangle \right|^2 \propto \sum_n \left| A_m(-\xi_n) \right|^2 \left| T(\xi_n) \right|^2 . \quad (34)$$

In this case the subscript m represents a realization of the experiment with a particular sensing matrix displayed on the SLM with $n = 1, \ldots, N$, where N is the number of pixels in the SLM. Furthermore, $\hat{E}^{(+)}(x_1)$ and $\hat{E}^{(+)}(x_2)$ are the positive frequency parts of the electric-field operator at the detector positions x_1 and x_2 in the signal and idler arms, respectively. In this case, the correlation function C_m is determined by the product of the sensing matrix A_m with the transmission function T that describes an arbitrary object. The evolution of the operators $\hat{E}^{(+)}(x_1)$ and $\hat{E}^{(+)}(x_2)$ through the experimental setup in figure 20(a) can be obtained through mathematical transfer functions. The transfer functions describe the propagation of the transverse profile of optical beams through the experiment. The field operators in equation (34) contain information of the sensing matrix and the object displayed on the SLM. In this case, the correlation between signal and idler modes can be rewritten as the product of matrices $C = AT$ by expressing $|A_m(-x_n)|^2$ as $A_{m,n}$ and $|T(x_n)|^2$ as T_n. Thus, the presence of quantum correlations in the degrees of freedom of position and momentum allows one to employ CS techniques to form the image of an object through the use of photons that never interacted directly with it. Furthermore, CS allows one to retrieve images by using only a small fraction of the total measurements required for raster scanning. For example, the image shown in figure 20(b) was reconstructed using using 27% of the measurements required in conventional raster scan techniques. The particular CS algorithm used in this experiment makes use of a discrete cosine transforms that exploits the sparsity of the Greek letter Ψ in this conjugate space. As shown in figure 20(c), the discrete cosine transform allows the identification of the pixels that provide essential information of the object, remarkably, figure 20(c) demonstrates that only few pixels convey relevant information about the object. This implies that it is possible to retrieve a good approximation of the Greek letter Ψ with fewer measurements.

5.2. Compressive object identification with entangled photons

The demonstration provided by Zerom in 2011 not only motivated an important number of schemes for quantum imaging but triggered the possibility of building quantum protocols for remote sensing and object identification [12, 72, 74].

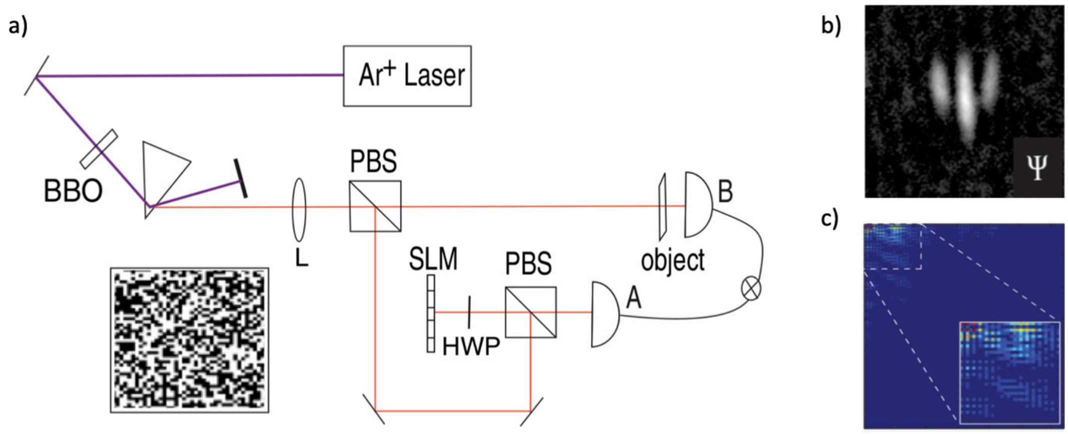

Figure 20. Schematic of entangled-photon compressive ghost imaging (a). Here CS techniques are used to avoid pixel-by-pixel raster scan, the experimental reconstruction of the Greek symbol Ψ is shown in (b). The sparsity of the symbol is observed in the space of spatial frequencies, see (c). Reprinted with permission from [70].

For example, in 2013, Magaña-Loaiza and colleagues demonstrated object tracking using entangled photons [72]. The team introduced a CS protocol that tracks a moving object by removing static components from a scene. This protocol was carried out on a quantum imaging scheme to minimize both the number of photons and the number of measurements required to form a quantum image of the tracked object. This procedure tracks an object at low light levels with fewer than 3% of the measurements required for a raster scan, leading to an effective use of the information content in each photon.

The experimental setup for object tracking is shown in figure 21(a). Entangled photons are generated in a bismuth barium borate (BiBO) crystal through a type-I SPDC process. The far-field of the BiBO crystal is imaged onto two DMDs with a lens and a BS. One DMD is used to display a scene with the object to be tracked, while the other is used to display the CS random binary patterns. Single-photon counting modules are used for joint detection of the signal and idler photons.

This scheme for correlated imaging relies on the simultaneous detection of photon pairs reflected off a changing scene O and a series of random matrices A_m. Similarly to the previous protocol, the subindex m indicates the mth realization of the experiment. The coincidence counts between the two detectors are given by

$$J_m \propto \int \mathrm{d}\hat{\rho}_{\mathrm{DMD}} \left| A_m \left(\frac{\hat{\rho}_{\mathrm{DMD}}}{m_r} \right) \right|^2 \left| O \left(\frac{-\hat{\rho}_{\mathrm{DMD}}}{m_0} \right) \right|^2, \qquad (35)$$

where A_m and O are the reflectivity functions displayed on the DMD_g located in the ghost arm and on DMD_o in the object arm, respectively. Meanwhile m_r and m_o are their corresponding image magnification factors. These are determined by the ratio of the distance between the nonlinear crystal to the lens and the distance from the lens to DMD_g or DMD_o.

CS uses optimization to recover a sparse n-dimensional signal from a series of m incoherent projective measurements, where the compression comes from the fact that $m < n$ [94]. This protocol for compressive object tracking allows one to identify a moving object in a scene by discarding static pixels. A scene with a moving object possesses static elements that do not provide information about the object's motion or trajectory. These redundancies can be discriminated from the moving object as follows. Let us consider the projection of two different frames onto the same pseudorandom pattern. Each projective measurement picks up little information about the components of a frame. If the two projective measurements produce the same correlation value, it would imply that the two frames are identical and meaningless information is being retrieved. The opposite case would reveal information about the changes in a scene. This protocol is formalized as follows. Two different correlation vectors, J^j and J^{j-1}, corresponding to two consecutive frames are subtracted, giving ΔJ. This introduces the following important modification to equation (33).

$$\min_{\Delta O'} \|\nabla(\Delta O')\|_{\ell_1} + \frac{\mu}{2} \|\Delta J - A\Delta O'\|^2_{\ell_2}. \qquad (36)$$

The algorithm known as total variation minimization by augmented Lagrangian and alternating direction (TVAL3) allows one to solve the aforementioned problem [99]. The subtracted vector ΔJ is sparser than both J^j or J^{j_1}, thus requiring fewer measurements for its reconstruction. This corresponds to fewer realizations of A_m, and hence a smaller sensing matrix A. Furthermore, subtracting the background in this manner mitigates the presence of environmental noise during the tracking process. In this case, the retrieved image $\Delta O'$ provides information about the relative changes in the scene. This is shown in figures 21(b)–(g).

This protocol uses CS to exploit the sparsity existing between two realizations of a scene with a moving object [72]. It also reduces the environmental noise introduced during the measurement process. In addition, it enables the fast retrieval of images by means of single-pixel detectors.

5.3. Digital spiral object identification

In addition to photon correlations in the variables of linear position and linear momentum, one can utilize correlations in the conjugate variables of ANG and OAM to perform object identification and remote sensing [49, 100] . In 2005, Torner, Torres and Carrasco proposed the possibility of using

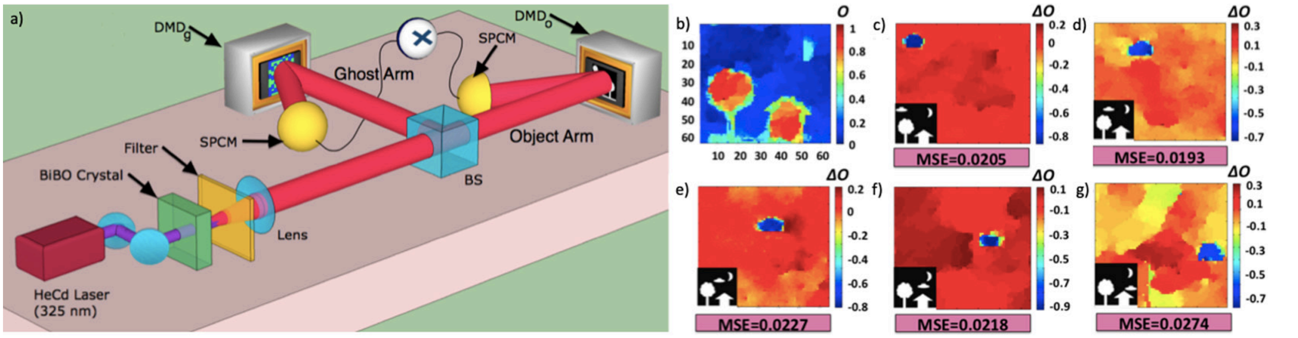

Figure 21. Compressive object tracking with entangled photons. A laser is used to pump a BiBO crystal that produces entangled photon pairs in the variables of linear position and linear momentum. (a) One of the down-converted photons illuminates a DMD where a scene with a moving object is displayed, the other conjugate photon illuminates a DMD where CS is implemented. Two single-photon detectors are used to measure photons reflected from the DMD. Compressed ghost image of (b) the background of the scene and (c)–(g) the tracked object at different positions. Reprinted with permission from [72].

the OAM spectrum of a light beam to perform imaging, they called this technique spiral object identification [101]. This idea motivated multiple schemes in which the spiral spectrum of light and OAM correlations are used to perform remote sensing [12, 74, 102, 103]. The group of Miles Padgett used OAM correlations to demonstrate holographic ghost imaging for phase objects [102]. In 2013, a team led by Alexander Sergienko used OAM correlations to perform object identification [12]. More recently, Chen and Romero demonstrated a quantum version of the spiral imaging using entangled OAM states [103].

In 2016, Magaña-Loaiza *et al* demonstrated that intensity fluctuations give rise to the formation of correlations in the OAM components and ANGs of random light [73]. Interestingly, the spatial signatures and phase information of an object with rotational symmetries can be identified using classical OAM correlations in random light [74]. The Fourier components imprinted in the digital spiral spectrum of the object, as measured through intensity correlations, unveil its spatial and phase information. Sharing similarities with conventional CS protocols that exploit sparsity to reduce the number of measurements required to reconstruct a signal, this technique allows sensing of an object with fewer measurements than other schemes that use pixel-by-pixel imaging.

The experimental implementation of digital spiral object identification is shown in figure 22(a), a laser beam illuminates a DMD that is used to generate pseudothermal light. The BS produces two copies of the thermal beam, one of the two beams illuminates the object described by the transmission function $\Gamma(r,\phi)$. In addition, a series of OAM projections are performed in each of the beams by means of a SLM. As shown in figure 22(a), a SLM is used to project random fields of light into specific OAM modes. Furthermore, a second SLM is used in the other arm to display the object to be identified and to perform OAM projections. This is achieved by multiplying the object by a forked diffraction grating. The protocol is formalized by performing intensity correlations between the two arms of the experiment. The second-order correlation function that describes intensity correlations in the OAM domain is defined as

$$\Delta G^{(2)}(\ell_r,\ell_t) = \left| \int r\mathrm{d}r\mathrm{d}\phi \overline{|E(\rho,\phi)|}^2 \Gamma(\rho,\phi)\frac{\mathrm{e}^{\mathrm{i}\Delta\ell\phi}}{2\pi} \right|^2, \tag{37}$$

where $\Delta\ell = \ell_t - \ell_r$, and the overbar means ensemble average. As shown in figures 22(b)–(g), the technique is tested with objects with four- and six-fold rotational symmetries. Each object is encoded onto the SLM located in the test arm.

A series of OAM projections is performed in each arm to construct a 2D matrix with the normalized second-order correlation function, see figures 22(c) and (d). The OAM number in the test and reference arms are denoted by ℓ_t and ℓ_r, respectively. The normalized second-order OAM correlation function is calculated by $g^{(2)}(\ell_r,\ell_t) = \langle I_{\ell_r} I_{\ell_t}\rangle / \langle I_{\ell_r}\rangle\langle I_{\ell_t}\rangle$, where $\langle I_{\ell_r} I_{\ell_t}\rangle$ is proportional to the coincidence count rate.

As shown in figures 22(c) and (f), an amplitude object with N-fold rotational symmetry imprints its Fourier components into the second-order OAM correlation matrix. The correlation signal is high along the diagonal elements of the matrix, where $\Delta\ell = \ell_t - \ell_r = \pm N$ due to the symmetry of the amplitude object. These signatures can be observed when $\Delta\ell = \pm 4$, for the object with fourfold rotational symmetry, and when $\Delta\ell = \pm 6$, for the object with sixfold rotational symmetry. Consequently, it is evident that one can use the OAM correlation matrix to identify the two objects. Furthermore, note that this technique requires a small number of measurements compared to traditional imaging schemes that rely on pixel-by-pixel raster scanning.

In figures 22(d) and (g), the transverse sections are plotted for the correlation matrices in figures 22(c) and (f), respectively. For simple and symmetric objects, a single line in the correlation matrix can provide adequate information about the object. However, the measurement of the total OAM correlation matrix is required for complicated objects that lack rotational symmetry [12, 74].

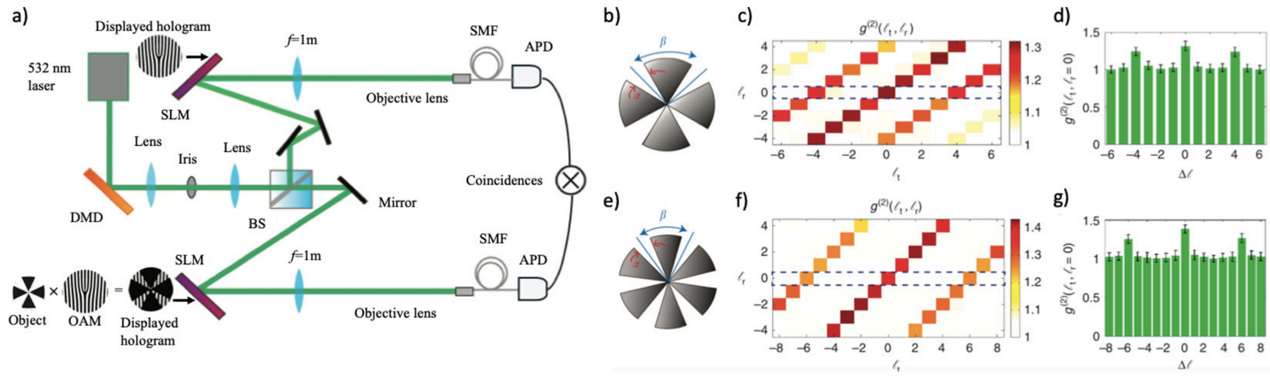

Figure 22. (a) Experimental setup utilized for digital spiral object identification with random fields of light. The SLM in the upper arm projects the random field of light into specific OAM modes, whereas, the second SLM in the lower arm is used to display objects and to perform OAM projections. This protocol was utilized to identify the objects in (b) and (e). The correlation matrices for the objects are shown in (c) and (f), respectively. The rows denoted by the dotted boxes in (c) and (f) are shown in (d) and (g), respectively. Reprinted with permission from [74].

One remarkable advantage of this technique is that it does not require the preparation of fragile quantum states of light and operates at both low- and high-light levels. In addition, it is robust against environmental noise, a fundamental feature of any realistic scheme for remote sensing.

6. Quantum metrology and quantum state tomography

The spatial profile of light has been utilized to measure small physical parameters with unprecedented precision and to encode multiple bits of information for quantum information tasks [8, 25, 31, 40, 104, 105]. Now we discuss quantum protocols for metrology that use the spatial profile of light to measure transverse displacements [82, 83, 107, 109]. We then turn our attention to review schemes for characterization of spatial photonic states that reside in high-dimensional Hilbert spaces [8, 110].

6.1. Quantum-enhanced metrology

The use of photons to measure small physical quantities represents one of the most important applications of light [2]. The quantum mechanical properties of light have been recognized as useful resources to surpass fundamental limits of protocols for classical metrology [111]. Interestingly, the potential of these nonclassical resources gave birth to the field of quantum-enhanced metrology [2, 111]. Here, we briefly discuss schemes that use spatial entanglement to measure small transverse displacements.

As discussed above, the conservation of momentum in SPDC processes gives rise to the generation of entangled states in the conjugate variables of ANG and OAM [27, 49]. In the past two decades, the OAM of light has become an important resource for the measurement of small angular displacements [8, 25, 31, 40, 104, 105]. The interest in using beams of light carrying OAM for measurement of angular rotations started with the work from Courtial and co-workers in which the physics behind rotational frequency shifts is described [107]. These protocols were then combined with entangled states of light such as NOON states to perform accurate estimations of angular rotations. NOON states are path-entangled states that are a coherent superposition of N photons path 1 and 0 photons in path 2, and 0 photons path 1 and N photons in path 2 [5]. This interesting combination led to a new form of photonic states in the azimuthal degree of freedom that are called photonic gears and are used for ultra-sensitive measurements of angular rotations [82, 83, 108].

In 2011, Kumar *et al* investigated the potential of exploiting entangled photons carrying OAM to increase the resolution and sensitivity of classical interferometric measurements of angular displacements [82]. In this protocol, a Dove prism induces a transverse angular rotation of a light beam. The possibility of using nonclassical fluctuations of light to surpass the noise properties that characterize laser beams is called supersensitivity [111]. Furthermore, the frequency of the fringes formed by multiphoton interference oscillates faster than those produced by laser light under equivalent circumstances, this feature is also a form of superresolution. The interferometric arrangement studied by Kumar is shown in figure 23. In this case, multiphoton interference in a Mach–Zehnder interferometer is used to estimate the rotation of a Dove prism.

The nonlinear interaction in the process of SPDC leads to the generation of the following high-dimensional state with multiple photons, sometimes called two-mode squeezed vacuum state [34, 58, 112]

$$|\Phi\rangle = |\Phi_0\rangle + |\Phi_2\rangle + |\Phi_4\rangle + ... \quad (38)$$

The first term $|\Phi_0\rangle$ is a vacuum state, the second term $|\Phi_2\rangle$ describes the simultaneous generation of two photons, one in each of the two modes, and the third term $|\Phi_4\rangle$ describes the probability amplitude of generating four photons, in this case, two photons in the signal mode and two in the idler mode. The probability of generating four photons is orders of magnitude smaller than the probability of generating two photons. The two-photon state in the azimuthal basis can be written as

$$|\Phi_2\rangle = \sum_{\ell} \varrho_\ell |\ell\rangle_s |-\ell\rangle_i, \quad (39)$$

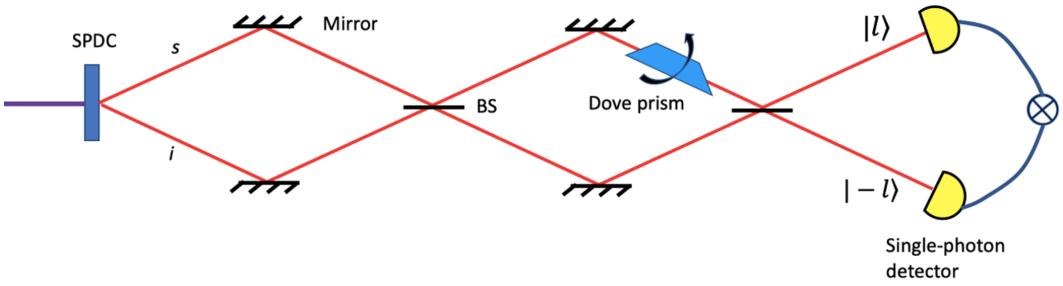

Figure 23. Experimental arrangement for estimation of angular rotations using entangled states endowed with OAM. Entangled OAM states are produced by the process of SPDC, entangled photons are injected into a Mach–Zehnder interferometer that contains a Dove prism. The photons emerging through the output port of the interferometer are measured by two SLMs and single-photon detectors. The purpose of this protocol is to estimate the angular rotation of the Dove prism with high sensitivity.

where ϱ_ℓ is the probability amplitude of generating a signal and idler photons with the OAM values of $\ell\hbar$ and $-\ell\hbar$ respectively. Similarly, the four-photon state is described as

$$|\Phi_4\rangle = \sum_{\ell,\ell'} \varrho_{\ell,\ell'}|\ell,\ell'\rangle_s|-\ell,-\ell'\rangle_i. \tag{40}$$

$\varrho_{\ell,\ell'}$ describes the probability ampitude that two photons with OAM values ℓ and ℓ' are produced in the signal mode, and two photons with OAMs $-\ell$ and $-\ell'$ are produced in the idler mode.

As shown in figure 23, signal and idler modes are injected in the two input ports of a Mach–Zehnder interferometer containing a Dove prism in one of the arms. The photons emerging through the upper output port of the interferometer are projected onto different OAM modes $|\ell\rangle$, whereas the photons emerging through the lower port are projected onto $|-\ell\rangle$. The OAM projected measurement is performed through the experimental setup shown in figure 3. The protocol is concluded by performing photon correlations between the two output ports of the interferometer. For this particular case in which post-selection is implemented between two modes, the interference pattern as a function of the angle of the Dove prism θ is described as

$$\langle\Phi_2|\Phi_2\rangle = \frac{1}{2}\mathrm{Cos}^2(2\ell\theta). \tag{41}$$

In this case, the uncertainty in the estimation of the angular rotation $\Delta\theta$ is given by

$$\Delta\theta = \frac{\langle\Delta\hat{P}\rangle}{\partial\langle\Delta\hat{P}\rangle/\partial\theta} = \frac{1}{4\ell}. \tag{42}$$

The expectation value of the measurement operator $\hat{P}$, is $\langle\hat{P}\rangle = \mathrm{Tr}[\hat{P}|\Pi_2^\ell\rangle\langle\Pi_2^\ell|]$, where the post-selected state $|\Pi_2^\ell\rangle$ is given by $-\frac{1}{2\sqrt{2}}[1+\mathrm{e}^{4\mathrm{i}\ell\theta}]|1\rangle_{+\ell}|1\rangle_{-\ell}$, the post-selected state $|\Pi_2^\ell\rangle$ can be implemented by measuring coincidences of photons with opposite values of OAM. This expression can be generalized for a case in which N entangled photons carrying a ℓ value of OAM are utilized. In this case, the uncertainty in the measurement of an angular rotation $\Delta\theta$ scales as $\frac{1}{2N\ell}$. Interestingly, the uncertainty in the measurement decreases with the number of entangled photons and the OAM value of the photons. Remarkably, the sensitivity in the estimation of an angular rotation using classical states, such as a coherent states, scales with $\frac{1}{2}\sqrt{N}\ell$, which is known as the shot noise limit. In this case, N represents the number of detected photons.

This work triggered other protocols for the estimation of angular rotations. For example, Magaña-Loaiza *et al* demonstrated the use of weak values for estimation of angular rotations [109]. In addition, D'Ambrosio and colleagues implemented an experimental protocol for quantum metrology that relies on the use of NOON-like states with high values of OAM [83]. Sharing similarities with Kumar's protocol [82], this scheme enables amplification of mechanical angular rotations by means of light beams with high values of OAM. In this scheme, a device known as a q-plate maps a polarization state into an OAM state with different polarization properties [113]. The q of the liquid crystal plate determines the OAM values of the photons that pass through the plate, and consequently the amplification of the rotation, this is illustrated in figure 24 [83]. Here a single photon passes through a q-plate and a half wave plate (HWP) to generate coherent superposition of OAM states with different polarizations. A physical rotation induces a relative phase between the states with right- and left-circular polarizations that lead to an amplification of the angular rotation by a factor of $m = 2q + 1$. The two replicas are then combined to form interference fringes in the azimuthal profile of the beam. The density of the fringes scale with ℓ, enabling a high-resolution measurement of angular rotations.

6.2. Quantum state tomography for high-dimensional photonic wavefunctions

The challenges involved in the process of extracting large amounts of information, encoded in photonic wavefunctions, impose practical limitations to realistic quantum technologies [8, 25, 110]. A family of techniques classified under the umbrella of quantum state tomography offers the possibility of decoding information from light particles [7, 8, 32, 114, 115]. The spatial profile of light enables the possibility of encoding information [25]. For this reason, there has been an important interest in developing non-conventional techniques to fully characterize spatial states of light. Alternative techniques for state tomography are motivated by the unfeasible number of projective measurements required to characterize quantum states using conventional techniques [7, 8]. In general, the

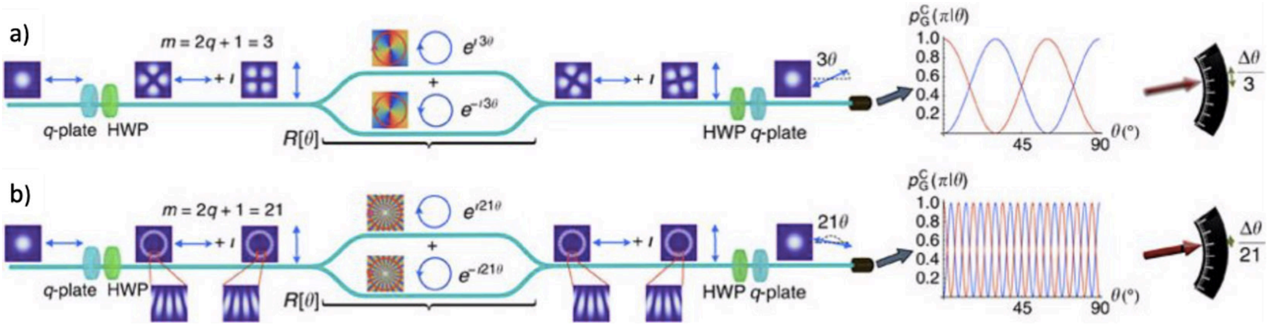

Figure 24. (a) Photonic polarization gears for sensitive measurements of angular displacements. In this case, a physical rotation is identified by using interference between photons with $\ell = 3$, see (a). As shown in (b), the resolution of the protocol can be improved by using light endowed with higher values of OAM. Reprinted with permission from [83].

number of measurements scales quadratically with the dimension size of the state. In recent years, the use of direct measurement has enabled the implementation of optimization algorithms that offer the possibility of reducing the number of measurements to reconstruct the density matrix of a spatial state of light [7]. For example, Knarr and co-workers recently performed measurement of high-dimensional phase-spaces via CS [42]. The team demonstrated compressive measurement of the Dirac distribution for photonic states with different degrees of coherence. Interestingly, the Dirac distribution provides equivalent information to the density matrix [116].

6.3. CS for quantum state characterization

We now describe recent experiments related to the direct measurement of the wavefunction. We start this section by introducing a technique called compressive direct measurement (CDM) [8]. In this protocol, Mirhosseini and colleagues combine the benefits of direct measurement with CS [7, 8]. In this scheme, the polarization degree of freedom of the photon is coupled to its unknown spatial target profile. The initial state can be written as

$$|\Omega\rangle = |\Upsilon\rangle|V\rangle = \sum_{i=1}^{N} \Upsilon_i |x_i\rangle|V\rangle, \tag{43}$$

where $|V\rangle$ indicates that the initial polarization is vertical and where $|\Upsilon\rangle$ is the spatial unknown wavefunction that will be characterized. Then, a series of random weak measurements are performed in order to retrieve the spatial wavefunction $|\Upsilon\rangle$. Each measurement is described by the projection operator $\hat{Q}_m$, that can be expanded as a weighted sum of position projection operators $\hat{\pi}_j$ at all the points $\hat{Q}_m = \sum_j Q_{m,j}\hat{\pi}_j$. In this case, the binary coefficient $Q_{m,j}$ is real and can be either 0 or 1. The state of the particle after the measurement can be approximately described as

$$\mathrm{e}^{\mathrm{i}\alpha}|\Omega\rangle \approx |\Omega\rangle + \alpha \sum_{i=1}^{N} Q_{m,j}\Upsilon_i |x_i\rangle|H\rangle. \tag{44}$$

Following the weak measurement, a strong projective measurement onto the zeroth order momentum state is performed. This measurement destroys the spatial structure of the photons, producing a beam with the polarization state

$$|s_m\rangle = |V\rangle + \frac{\alpha}{\phi_0\sqrt{N}} \sum_j Q_{m,j}\Upsilon_j |H\rangle. \tag{45}$$

At this stage the information about the state-vector Υ_j is encoded in the expected values of the polarization of the post-selected state

$$\begin{aligned} \bar{\sigma}_{x,m} &= \langle s_m|\hat{\sigma}_x|s_m\rangle = k\sum_j Q_{m,j}\Re[\Upsilon_j], \\ \bar{\sigma}_{y,m} &= \langle s_m|\hat{\sigma}_y|s_m\rangle = -k\sum_j Q_{m,j}\Im[\Upsilon_j], \end{aligned} \tag{46}$$

where $\hat{\sigma}_x = |H\rangle\langle V| + |V\rangle\langle H|$, $\hat{\sigma}_y = -\mathrm{i}|H\rangle\langle V| + \mathrm{i}|V\rangle\langle H|$ and $k = \frac{2\alpha}{\phi_0\sqrt{N}}$. After repeating the measurement M times, one obtains a linear relation between the measurement results and the unknown wavefunction

$$\begin{pmatrix} \Xi_1 \\ \Xi_2 \\ \vdots \\ \Xi_M \end{pmatrix} = \begin{pmatrix} Q_{1,1} & Q_{1,2} & \cdots & Q_{1,N} \\ Q_{2,1} & Q_{2,2} & \cdots & Q_{2,N} \\ \vdots & \vdots & \ddots & \vdots \\ Q_{M,1} & Q_{M,2} & \cdots & Q_{M,N} \end{pmatrix} \begin{pmatrix} \Upsilon_1 \\ \Upsilon_2 \\ \vdots \\ \Upsilon_N \end{pmatrix}. \tag{47}$$

Here, $\hat{\Xi}_m = \frac{1}{k}[\bar{\sigma}_{x,m} - \mathrm{i}\bar{\sigma}_{x,m}]$, and $m \in 1:M$and $n \in 1:N$, where M is the number of times the measurement is repeated with different random projections. For the case where $M = N$, the solutions of the system above can be exactly solved for a non-singular matrix $\hat{Q}$. However, for the case when $M \leqslant N$ there exists multiple solutions to the system of equations.

CS provides a method for finding the solution by using the prior knowledge of sparsity of the unknown function in a known basis. This is often achieved by solving an optimization problem that can be formulated in multiple forms. One possibility is to assume sparsity in the gradient basis, which leads to the following optimization problem

$$\min_{\hat{\Upsilon}'} \|\nabla\hat{\Upsilon}'\|_{\ell_1} + \frac{\mu}{2}\|\hat{Q}\hat{\Upsilon}' - \hat{\Xi}\|^2_{\ell_2}. \tag{48}$$

Similar to equation (33), the solution of the optimization problem allows the determination of the smoothest state $\hat{\Upsilon}'$, that is approximately in agreement with the experimental data.

Figure 25(a) shows the schematic of the experiment. A vertically polarized Gaussian beam illuminates a SLM, which together with two quarter wave plates (QWPs) labeled as WP1

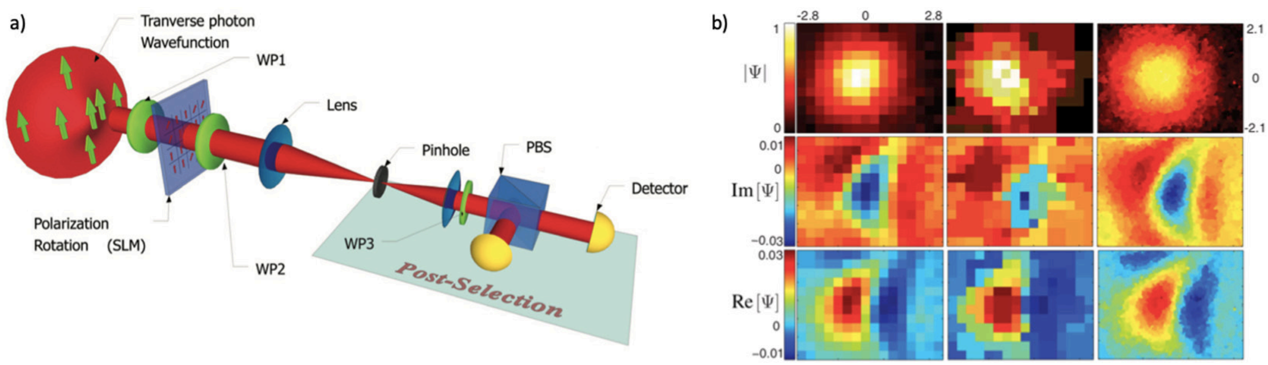

Figure 25. (a) a collimated vertically polarized Gaussian beam illuminates a SLM, which is used along with two quarter wave plates (WP1and WP2) to rotate the polarization at each pixel. A lens focuses the beam onto a pinhole with a diameter of 10 μm. The polarization measurement is performed on the light collected from the pinhole using a quarter wave plates/half wave plates (WP3) and a PBS. (b) the amplitude, real, and imaginary parts of an aberrated Gaussian state measured experimentally. The left column shows data from a pixel-by-pixel scan of the state for $N = 192$. The middle column presents the reconstructed wavefront for $N = 192$, and $M/N = 20\%$ of total measurements from the CDM method. The right column demonstrates reconstruction of a higher dimensional state for $N = 19\,200$, and $M/N = 20\%$ of total measurements. Reprinted with permission from [8].

and WP2 performs the polarization rotation. The amount of rotation can be controlled at each pixel by setting the gray-scale values on the SLM. After the Fourier transforming lens, the post-selection in the momentum basis is performed by using a pinhole that projects on a single spatial mode. The real part of the wavefunction is retrieved by using a HWP (shown as WP3 in figure 25) and a PBS. Similarly, the imaginary part of the wavefunction is measured by using a QWP before the PBS. The flux of photons at the two output ports of the PBS are detected with APDs.

For each measurement m, a pre-generated random binary matrix $\hat{Q}_m$ is displayed on the SLM. The photon fluxes measured at the APDs are used to find the expectation values of the Pauli matrices in equation (46) for each measurement. The wavefunction is then retrieved via post processing on a computer.

The technique is used to measure an aberrated Gaussian beam, see figure 25(b). The wavefunction is reconstructed via standard direct measurement. The real and imaginary parts from a pixel-by-pixel raster scan are shown on the left column of figure 25(b) for an $N = 12 \times 16 = 192$ dimensional Hilbert space. On the middle column, it is shown the real and imaginary parts of the wave function reconstructed from CDM using $N = 192$ and $M/N \times 100 = 20\%$. It is evident that a reconstruction with 20% of measurements can find all the main features of the wavefunction. The increased sampling results in a more sparse representation in the gradient basis. On the right column of figure 25(b), the reconstructions for $N = 120 \times 160 = 19\,200$ and $M/N \times 100 = 20\%$ are shown. In this case an experiment with 20% of measurements provides an accurate reconstruction.

In a similar spirit, it has been demonstrated the use of CS for entanglement imaging, measurement of spatial wavefunctions, and characterization of high-dimensional entangled states in the variables of position and momentum. Recently, compressive characterization of telecom photon pairs in the spatial and spectral degrees of freedom was demonstrated [110]. This technique utilizes a series of random projective measurements in the spatial basis that do not perturb the spectral properties of the photon. The sparsity in the spatial properties of down-converted photons allows the efficient implementation of CS to reduce the number of measurements to reconstruct spatial and spectral properties of correlated photon pairs at telecom wavelength. This protocol opens the possibility of increasing and exploiting the complexity and dimensionality of quantum protocols that utilize multiple degrees of freedom of light with high efficiency.

As discussed before, the process of SPDC produces photons correlated in multiple degrees of freedom. The spatial and spectral properties of these photons define high-dimensional Hilbert spaces described by the following state:

$$|T\rangle = \sum_{\omega=1}^{D_\omega} f_\omega |\omega\rangle_s |\omega\rangle_i \otimes \sum_{j=1}^{D_j} s_j |x_j\rangle_s |x_j\rangle_i, \tag{49}$$

where f_ω represents the probability amplitude of finding signal and idler in the frequency mode $|\omega\rangle_{s,i}$ Similarly, the spatial degree of freedom is described by a coherent superposition of spatial (‘pixel’) states $|x_j\rangle_{s,i}$; the probability of finding a photon pair in these states is described by the coefficient s_j. The general state in equation (49) can be characterized by performing a series of random projective measurements on photons emerging from long optical fibers that allows one to map the spectral content of the photons to time bins. A series of photon number correlations for all the time bins are utilized to solve a similar optimization problem to the one in equation (48), this solution leads to an approximation of the state in equation (49).

As shown in figure 26(a), a pulsed laser pumps a PPKTP waveguide, that produces correlated photon pairs at telecom wavelengths [31]. This type-II PPKTP waveguide produces telecom photons with orthogonal polarizations. The generated down-converted photons illuminate a DMD that is used to measure their spatial properties. The downconverted photon pairs are then separated by a PBS and coupled into long single-mode fibers that map frequency to time of arrival.

The joint arrival time of SPDC photons is shown in figure 26(b). The marginals are estimated by taking the transfer function of the arrival time of the downconverted photons.

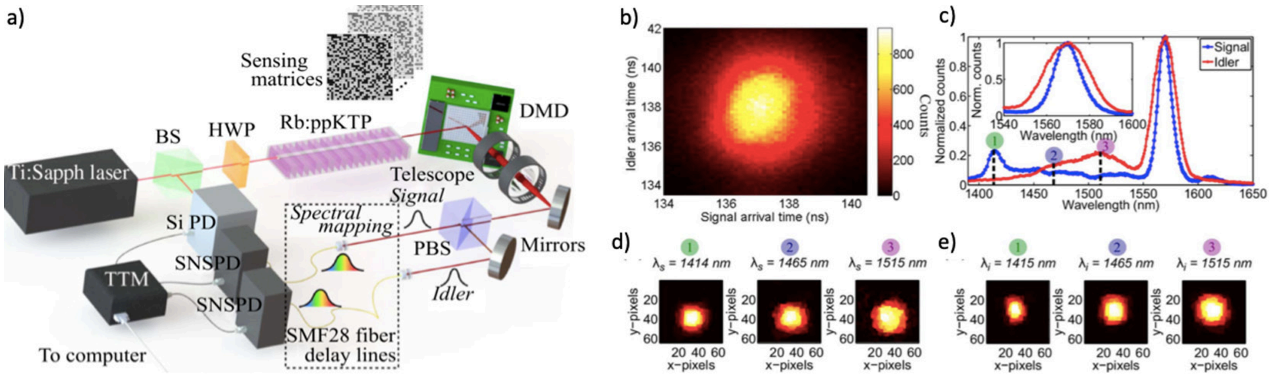

Figure 26. (a) Experimental apparatus used for the compressive characterization of telecom photon pairs in the spatial and spectral degrees of freedom. (b) shows the joint arrival time of SPDC photons. The measured spectra of the photon pairs is shown in (c). The insets in (d) and (e) show the spatial profile of photons at the satellite peaks in (c). Reprinted with permission from [110].

The resulting spectra of both photons are shown in figure 26(c). The nonlinear crystal is designed to show a phase-matching peak at 1570 nm, which corresponds to the main peak in the spectrum. The spatial profiles for satellite peaks a at an intermediate walenghts are shown in the insets of figures 26(d) and (e).

The complex photonic states measured with these techniques would require unfeasibly large acquisition times with other conventional techniques [8, 42, 110]. The dramatic reduction in the number of measurements required to characterize high-dimensional states and SPDC sources make these techniques a powerful diagnostic tool for quantum photonic protocols. The simplicity and robustness of these techniques enable the identification of experimental conditions that limit the performance of quantum protocols that rely on efficient quantum interference.

7. Quantum information with high-dimensional photonic states

The use of optical pulses of light through optical fibers has played a tremendous impact in the way modern society communicates [40, 104–106]. However, the capacity of multiple communication protocols, such as internet, are reaching their limits in terms of data traffic capacity. This limitation in classical communication protocols has triggered new classical and quantum schemes for communication as well as secure schemes for distribution of quantum information. In this section, we discuss recent approaches that exploit multiple degrees of freedom of light to boost the data-carrying capacity of protocols for optical communication in free-space and fibers.

7.1. Quantum communication with high-dimensional states of light

In the past ten years, there has been a strong impetus in using new degrees of freedom of light that offer the possibility of surpassing information capacity limits of protocols that use polarization. In this regard, the engineering of spatial modes of light as simple as 'pixel' states have been used to transmit multiple bits of information in a single photon [25, 31, 40, 104, 105]. Furthermore, recent progress in liquid crystal devices has enabled the robust manipulation of the polarization and the spatial profile of light. These concepts have been extensively studied in free-space links by multiple groups [3]. However, recent progress in the engineering of photonic crystal fibers that support exotic beams of light endowed with OAM have motivated new research directions. Remarkably, these protocols have enabled information transmission at the impressive rate of 1.6 Tb per second [40, 104].

As discussed in the previous sections of this review, it is possible to engineer spatial modes of light for information encoding [117]. Given the maturity of techniques for measuring spatial modes carrying OAM, $LG_p^\ell(\rho, \phi, z)$ modes have been widely utilized in multiple studies [3, 25, 28]. A detailed review of this field can be found in [3]. Despite the enormous potential of spatial modes of light for optical communication, turbulence represents one of the major challenges in the implementation of optical communication protocols in free-space. This problem has been alleviated by implementing adaptive schemes with deformable mirrors [41]. Other approaches include the implementation of neural networks for pattern recognition [105].

Free-space OAM communication in intracity links have been demonstrated by multiple groups [3, 25, 28, 106]. In 2014, Krenn and colleagues implemented a classical communication protocol in a 3 km link of strong turbulence in the city of Vienna, see figure 27 [105]. In this experiment, the Austrian group demonstrated optical communication with 15 OAM modes, from $\ell = 0$ to $\ell = 15$. The transmitted modes were detected by a CCD camera and successfully identified with trained neural networks that led to an average error rate of approximately 1.7%. This protocol was utilized to transmit a gray-scale image of Mozart. This demonstration was implemented using a green laser with a wavelength of 532 nm.

Recent developments in photonic crystal fibers have enabled new protocols in which frequency, polarization and the spatial profile of light were utilized to dramatically increase the channel capacity of a communication protocol [40, 104]. In a recent experiment, a fiber link with 20 channels and 10 wavelength division multiplexers were utilized to multiplex

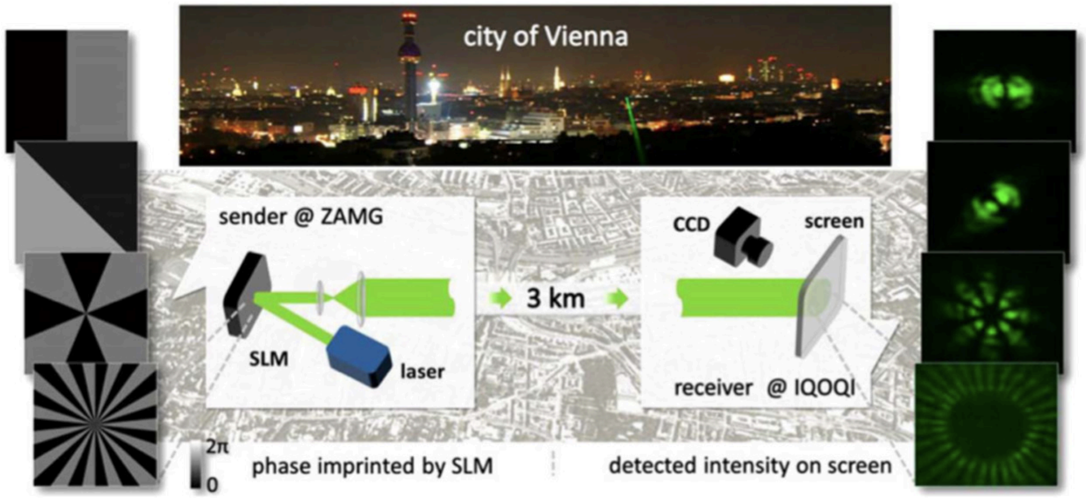

Figure 27. Experimental implementation of a high-dimensional free-space link across the city of Vienna. A series of holograms are prepared to define the alphabet of the communication protocol. These spatial modes are prepared by a SLM. The receiver uses a camera and neural networks to identify spatial beams of light such as those shown in the left panel of the figure. Reprinted with permission from [105] .

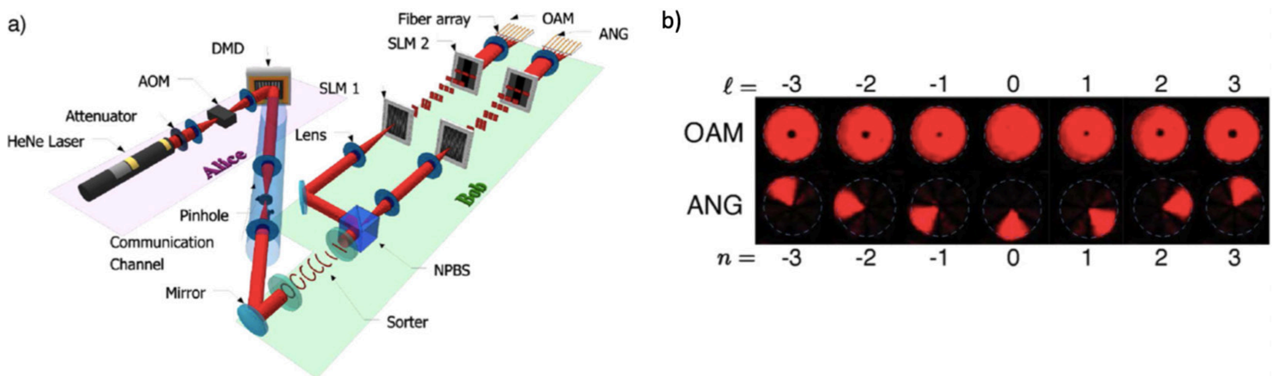

Figure 28. (a) The experimental implementation of high-dimentional quantum cryptography with spatial modes of light. Alice prepares the modes by carving out pulses from a highly attenuated He–Ne laser using an AOM. A DMD is used to impress spatial mode information on these pulses. Bob's mode sorter and fan-out elements map the OAM modes and the ANG modes into separated spots that are collected by an array of fibers. The images of the implemented alphabet of the two complementary spatial OAM and ANG bases are shown in (b). Reprinted with permission from [31].

two OAM modes with different polarization to demonstrate a transmission capacity of 1.6 Tb. A series of fiber-based implementations were then demonstrated with lower losses and higher fidelities [40].

7.2. High-dimensional quantum cryptography

Nowadays, there has been great interest in the development of means for secure communication that are based on the fundamental laws of quantum mechanics. Quantum key distribution (QKD) represents a remarkable example of secure quantum technologies. Similarly to other schemes for quantum communication, QKD utilizes quantum states to share information between two parties [38]. In 1984, Charles Bennett and Gilles Brassard proposed to use the polarization of photons to transmit information in a secure fashion, the ultimate goal of this protocol is to generate a sequence of numbers that acts as a quantum key to encrypt information [118], this protocol is known as BB84. Due to the dimensionality of the Hilbert space for polarization, only a single bit of information can be encoded in each photon [108]. As discussed in the first sections of this review, spatial modes of light, such as $LG_p^\ell(\rho, \phi, z)$ modes, can be used to construct high-dimensional spaces that enable the encoding of multiple bits of information in a single particle of light [25]. Furthermore, these protocols offer the possibility of increasing the robustness of secure protocols against intercept-resend eavesdropping attacks [3, 28]. In the particular implementation shown in figure 28(a), the OAM of photons and the corresponding MUBs of ANG are used to define a seven-dimensional alphabet encoded in these bases, see figure 28(b) [31]. In this scheme, the team demonstrated a channel capacity of 2.05 bits per sifted photon.

The conceptual experimental setup in figure 28(a) shows an attenuated He–Ne laser modulated by an acousto-optic modulator (AOM). The modulated pulse from the AOM illuminates a DMD that is used to prepare spatial modes. In this protocol, Alice initially picks a random sequence of desired OAM and ANG modes in the DMD's internal memory. The prepared spatial states are then imaged to Bob's receiving aperture via a $4f$-telescope that forms a lossless communication link. Bob's mode sorter consists of two refractive elements for performing a log-polar to cartesian transformation [119]. Going through these elements, an OAM mode is converted to a plane wave with a tilt that is proportional to the OAM mode index ℓ. A single lens focuses such a plane wave into a spot that is shifted by an amount proportional to ℓ. Similarly, an ANG mode transforms to a localized spot shifted by an amount proportional to the angular index n. A beam splitter is used to randomly choose between the OAM and ANG bases. Figure 28(b) shows the two complementary seven-dimensional bases used for information encoding.

The signals from single-photon detectors are processed by electronic circuits to produce photon counts using a gating signal that is utilized to synchronize events between Alice and Bob. The photon detection events are finally saved in Bob's computer. Alice and Bob are also connected via a classical link. After Alice and Bob collect a sufficiently large number of symbols, that are used to generate the quantum key, they stop the measurement. At this point, they publicly broadcast the bases used for preparation and measurement of each photon via the classical link. This step in the BB84 protocol utilizes classical communication between Alice and Bob. Alice and Bob then discard the measurements that were done in different bases. The key generated at this stage is referred to as the sifted key. After a series of filters and logic operations, the keys are transformed to a binary form on a symbol-by-symbol basis and randomized by means of a random-number generator shared by Alice and Bob. In this case, each of the spatial modes represents a symbol. After error-correction, Alice and Bob share two identical copies of the quantum key. Alice and Bob perform a post-selection procedure known as privacy amplification to minimize Eve's information. Finally, the secure key is used to securely transmit encrypted information over the classical channel. At this point, the QKD protocol is completed.

8. Perspectives

The impressive progress in the field of quantum imaging and information in the last two decades anticipates an imminent change in how society manages information. The possibility of using the laws of nature to encode multiple bits of information in a single photon or to transmit information in a secure fashion have had a tremendous social impact. These emerging technologies have transcended the scientific community, and nowadays the word 'quantum' is associated with enhancement or improvement. To some extent, these ideas are consequences of the enormous potential that proof-of-principle implementations of protocols for quantum imaging and information have demonstrated. We do not expect quantum technologies to replace classical technologies, however, we believe that the progress in the field of quantum photonic technologies will play a crucial role in the development of new hybrid devices in which the functionality of classical and quantum technologies is complemented.

Acknowledgments

We thank Ashan Ariyawansa and Chenglong You for helpful discussions.

ORCID iDs

Omar S Magaña-Loaiza https://orcid.org/0000-0003-4484-0258

References

[1] O'Brien J L, Furusawa A and Vuckovic J 2009 *Nat. Photon.* **3** 687–95
[2] Giovannetti V, Lloyd S and Maccone L 2011 *Nat. Photon.* **5** 222
[3] Willner A E *et al* 2015 *Adv. Opt. Photon.* **7** 66–106
[4] Aspuru-Guzik A and Walther P 2012 *Nat. Phys.* **8** 285–91
[5] Boto A N, Kok P, Abrams D S, Braunstein S L, Wiliams C P and Dowling J P 2000 *Phys. Rev. Lett.* **85** 2733
[6] Kok P, Munro W J, Nemoto K, Ralph T C, Dowling J P and Milburn G J 2007 *Rev. Mod. Phys.* **79** 135
[7] Lundeen J S, Sutherland B, Patel A, Steward C and Bamber C 2011 *Nature* **474** 188
[8] Mirhosseini M, Magana-Loaiza O S, Hashemi Rafsanjani S M and Boyd R W 2014 *Phys. Rev. Lett.* **113** 090402
[9] Howland G A, Lum D J and Howell J C 2014 *Opt. Express* **22** 18870
[10] Tsang M, Nair R and Lu X-M 2016 *Phys. Rev.* X **6** 031033
[11] Tham W-K, Ferreti H and Steinberg A M 2017 *Phys. Rev. Lett.* **118** 070801
[12] Uribe-Patarroyo N, Fraine A, Simon D S, Minaeva O and Sergienko A V 2013 *Phys. Rev. Lett.* **110** 043601
[13] Liberman L, Israel Y, Poem E and Silberberg Y 2016 *Optica* **2** 193
[14] Bialynicki-Birula I 1996 *Coherence and Quantum Optics VII* p 313
[15] Smith B J and Raymer M G 2007 *New J. Phys.* **11** 414
[16] Gerchberg R W and Saxton W O 1972 *Optik* **35** 237
[17] Fienup J 1982 *Appl. Opt.* **15** 2758
[18] Smithey D T, Beck M, Raymer M G and Faridani A 1993 *Phys. Rev. Lett.* **70** 1244
[19] Andrews D 2008 *Structured Light and Its Applications* (New York: Academic)
[20] Milonni P W and Boyd R W 2010 *Adv. Opt. Photon.* **4** 519
[21] Vallone G, D'Ambrosio V, Sponselli A, Slussarenko S, Marucci L, Sciarrino F and Villoresi P 2014 *Phys. Rev. Lett.* **113** 060503
[22] Beth R A 1936 *Phys. Rev.* **50** 115
[23] Bennett C H and Brassard G 1985 *Proc. IEEE* **28** 3153
[24] Shor P W and Preskill J 2000 *Phys. Rev.* **85** 441
[25] Yao A M and Padgett M P 2011 *Adv. Opt. Photon.* **2** 161
[26] Allen L, Beijersbergen M W, Spreeuw R J C and Woerdman J P 1992 *Phys. Rev.* A **45** 8185
[27] Mair A, Vaziri A, Weihs G and Zeilinger A 2001 *Nature* **412** 313
[28] Padgett M J 2017 *Opt. Express* **10** 11265
[29] Ali-Khan I, Broadbent C J and Howell J C 2007 *Phys. Rev. Lett.* **98** 060503
[30] O'Sullivan-Hale M N, Ali-Khan I, Boyd R W and Howell J C 2005 *Phys. Rev. Lett.* **94** 220501

[31] Mirhosseini M, Magana-Loaiza O S, O'Sullivan M N, Rodenburg B, Malik M, Lavery M P J, Padgett M J, Gauthier D J and Boyd R W 2015 *New J. Phys.* **17** 033033
[32] Kues M, Reimer C, Roztocki P, Romero-Cortes L, Sciara S, Wetzel B, Caspani L, Azana J and Morandotti R 2017 *Nature* **546** 622
[33] Dell'Anno F, De Siena S and Illuminati F 2006 *Phys. Rep.* **428** 53–168
[34] Pan J-W, Chen Z-B, Lu C-Y, Weinfurter H, Zeilinger A and Zukowski M 2012 *Rev. Mod. Phys.* **84** 777
[35] Dixon P B, Howland G A, Schneeloch J and Howell J C 2012 *Phys. Rev. Lett.* **108** 143603
[36] Shannon C E 1948 *Bell. Syst. Tech. J.* **27** 623
[37] MacKay D J 2000 *Information Theory, Interference, and Learning Algorithms* (Cambridge: Cambridge University Press)
[38] Nielsen M A and Chuang I L 2000 *Quantum computation and quantum information* (Cambridge: Cambridge University Press)
[39] Shannon C E 1951 *Bell. Syst. Tech. J.* **30** 50
[40] Bozinovic N, Yue Y, Ren Y, Tur M, Kristensen P, Huang H, Willner A E and Ramachandran S 2013 *Science* **340** 1545–8
[41] Rodenburg B, Mirhosseini M, Malik M, Magana-Loaiza O S, Yanakas M, Maher L, Steinhoff N K, Tyler G A and Boyd R W 2014 *New J. Phys.* **16** 089501
[42] Knarr S H, Lum D J, Schneeloch J and Howell J C 2018 *Phys. Rev.* A **98** 023854
[43] Martin L, Mardani D, Kondakci H E, Larson W D, Shanahang S, Jahromi A K, Malhotra T, Vamivakas A N, Atia C K and Abouraddy A F 2017 *Sci. Rep.* **7** 44995
[44] Hiesmayr B C, de Dood M J A and Loffler W 2016 *Phys. Rev. Lett.* **116** 073601
[45] Born M and Wolf E 1980 *Principles of Optics* (Oxford: Pergamon)
[46] Hanbury Brown R and Twiss R Q 1956 *Nature* **177** 27–9
[47] Einstein A, Rosen N and Podolsky B 1935 *Phys. Rev.* **47** 777
[48] Howell J C, Bennink N, Bentley S J and Boyd R W 2004 *Phys. Rev. Lett.* **92** 210403
[49] Leach J, Jack B, Romero J, Jha A K, Yao A M, Franke-Arnold S, Ireland D G, Boyd R W, Barnett S M and Padgett M J 2010 *Science* **329** 662–5
[50] Mandel L 1999 *Rev. Mod. Phys.* **71** 6861–97
[51] Scully M O, Englert B G and Walther H 1991 *Nature* **351** 111–6
[52] Magana-Loaiza O S *et al* 2016 *Nat. Commun.* **7** 13987
[53] Safari A, Fickler R, Giese E, Magana-Loaiza O S, Boyd R W and De Leon I 2019 *Phys. Rev. Lett.* **122** 133601
[54] Manzel R, Puhlmann D, Heuer D and Schleich W P 2012 *Proc. Natl Acad. Sci. USA* **109** 9314–9
[55] Rubinowicz A 1957 *Nature* **180** 160–2
[56] Rodenburg B, Mirhosseini M, Magana-Loaiza O S and Boyd R W 2014 *J. Opt. Soc. Am.* B **31** A51
[57] Knight P L 2005 *Science* **310** 631–2
[58] Loudon R 1983 *The Quantum Theory of Light* 2nd edn (Oxford: Clarendon)
[59] Gatti A, Brambilla E, Bache M and Lugiaton L 2004 *Phys. Rev. Lett.* **93** 093602
[60] Abellan C *et al* 2018 *Nature* **557** 212
[61] Molina-Terriza G, Torres J P and Torner L 2007 *Nat. Phys.* **3** 305–10
[62] Kwiat P G, Mattle K, Weinfurter H, Zeilinger A, Sergienko A V and Shih Y 1995 *Phys. Rev. Lett.* **75** 4337
[63] Boyd R W 2008 *Nonlinear Optics* 3rd edn (New York: Academic)
[64] Franke-Arnold S, Barnett S M, Yao E, Leach J, Courtial J and Padgett M 2004 *New J. Phys.* **6** 103
[65] Magana-Loaiza O S 2016 Novel effects in optical coherence: fundamentals and applications *PhD Thesis* University of Rochester
[66] Pittman T B, Shih Y H, Strekalov D V and Sergienko A V 1995 *Phys. Rev.* A **52** R3429
[67] Strekalov D V, Sergienko A V, Klyshko D N and Shih Y H 1995 *Phys. Rev. Lett.* **74** 3600
[68] Bennink R S, Bentley S J and Boyd R W 2002 *Phys. Rev. Lett.* **89** 113601
[69] Ferri F, Magatti D, Gatti A, Bache M, Brambilla E and Lugiato L A 2005 *Phys. Rev. Lett.* **94** 183602
[70] Zerom P, Chan K W C, Howell J C and Boyd R W 2011 *Phys. Rev.* A **84** 061894
[71] Howland G, Dixon P B and Howell J C 2011 *Appl. Opt.* **50** 5917
[72] Magana-Loaiza O S, Howland G A, Malik M and Boyd R W 2013 *Appl. Phys. Lett.* **102** 231104
[73] Magana-Loaiza O S, Mirhosseini M, Cross R M, Hashemi Rafsanjani S M and Boyd R W 2016 *Sci Adv.* **2** e1501143
[74] Zhang Y, Magana-Loaiza O S, Mirhosseini M, Zhou Y, Gao B, Hashemi Rafsanjani S M, Long G L and Boyd R W 2017 *Light Sci. Appl.* **6** e17013
[75] Kolobov M 2007 *Quantum Imaging* (Berlin: Springer) (ISBN:978-0-387-33988-7)
[76] Malik M, Magana-Loaiza O S and Boyd R W 2012 *Appl. Phys. Lett.* **101** 241103
[77] Refregier P and Javidi B 1995 *Opt. Lett.* **20** 767–9
[78] Clemente P, Duran V, Tajahuerce E and Lancis J 2010 *Opt. Lett.* **35** 2391–3
[79] Hong C K, Ou Z Y and Mandel L 1987 *Phys. Rev. Lett.* **59** 2044
[80] D'Angelo M, Chekhova M V and Shih Y 2001 *Phys. Rev. Lett.* **87** 013602
[81] Brida G, Genovese M and Berchera I R 2010 *Nat. Photon.* **4** 227–30
[82] Jha A K, Agarwal G S and Boyd R W 2011 *Phys. Rev.* A **5** 053829
[83] D'Ambrosio V, Spagnolo N, Re L D, Slussarenko S, Li Y, Kwek L C, Marrucci L, Walborn S P, Aolita L and Sciarrino F 2013 *Nat. Commun.* **4** 2432
[84] Monken C H, Souto Ribeiro P H and Padua S 1998 *Phys. Rev.* A **57** 3123
[85] Fonseca E J S, Monken C H and Padua S 1999 *Phys. Rev. Lett.* **82** 2868
[86] Edgar M W, Gibson G M and Padgett M J 2019 *Nat. Photon.* **13** 13–20
[87] Pirandola S, Bardahan B R, Gehring T, Weedbrook C and Lloyd S 2018 *Nat. Photon.* **12** 724–33
[88] Xiong J, Cao D-Z, Huang F, Li H-G, Sun X-J and Wang K 2005 *Phys. Rev. Lett.* **94** 173601
[89] Shih Y H and Alley C O 1988 *Phys. Rev. Lett.* **61** 2921
[90] Ekert A K 1991 *Phys. Rev. Lett.* **67** 661
[91] Clauser J F, Horne M A, Shimony A and Holt R A 1969 *Phys. Rev. Lett.* **23** 880
[92] Shapiro J H 2008 *Phys. Rev.* A **78** 061802
[93] Bromberg Y, Katz O and Silberberg Y 2009 *Phys. Rev.* A **79** 053840
[94] Baraniuk R G 2007 *IEEE Signal Process. Mag.* **24** 118–24
[95] Duarte M, Davenport M, Takhar D, Laska J, Sun T, Kelly K and Baraniuk R 2008 *IEEE Signal Process. Mag.* **25** 83–91
[96] Chan W L, Charan K, Takhar D, Kelly K F, Baraniuk R G and Mittleman D M 2008 *Appl. Phys. Lettt.* **93** 121105
[97] Morris P A, Aspden R S, Bell J E C, Boyd R W and Padgett M J 2015 *Nat. Commun.* **6** 5913
[98] Katz O, Bromberg Y and Silberberg Y 2009 *Appl. Phys. Lett.* **95** 131110
[99] Li C 2009 *MS Thesis* Rice University

[100] Franke-Arnold S, Barnett S M, Padgett M J and Allen L 2002 *Phys. Rev.* A **65** 033823
[101] Torner L, Torres J P and Carrasco S 2005 *Opt. Express* **13** 873
[102] Jack B, Leach J, Franke-Arnold S, Ritsch-Marte M, Barnett S M and Padgett M J 2009 *Phys. Rev. Lett.* **103** 083602
[103] Chen L, Lei J and Romero J 2014 *Light Sci. Appl.* **3** e153
[104] Wang J *et al* 2012 *Nat. Photon.* **6** 488
[105] Krenn M, Fickler R, Fink M, Handsteiner J, Malik M, Schedi T, Ursin R and Zeilinger A 2014 *New J. Phys.* **16** 113028
[106] Lavery M P *et al* 2015 *CLEO: Science and Innovations* **STu1L.4**
[107] Courtial J, Robertson D A, Dholakia K, Allen L and Padgett M J 2014 *Phys. Rev. Lett.* **112** 200401
[108] Potocek V, Miatto F M, Mirhosseini M, Magana-Loaiza O S, Liapis A C, Oi K L, Boyd R W and Jeffers J 2015 *Phys. Rev. Lett.* **115** 160505
[109] Magana-Loaiza O S, Mirhosseini M, Rodenburg B and Boyd R W 2014 *Phys. Rev. Lett.* **112** 200401
[110] Montaut N, Magana-Loaiza O S, Bartley T J, Verma V B, Nam S W, Mirin R P, Silberhorn C and Gerrits T 2018 *Optica* **5** 1418–23
[111] Lee H, Kok P and Dowling J P 2002 *J. Mod. Opt.* **49** 2325–38
[112] Magana-Loaiza O S, de J Leon-Montiel R, Perez-Leija A, U'ren A B, You C, Busch K, Lita A E, Nam S W, Mirin R P and Gerrits T 2019 *npj Quantum Inf.* **5** 80
[113] Slussarenko S, Murauski A, Du T, Chigrinov V, Marrucci L and Santamato E 2011 *Opt. Express* **19** 4085–90
[114] Choudhary S, Sampson R, Miyamoto Y, Magana-Loaiza O S, Hashemi Rafsanjani S M, Mirhosseini M and Boyd R W 2018 *Opt. Lett.* **43** 6101–4
[115] Mirhosseini M, Magana-Loaiza O S, Chen C, Hashemi Rafsanjani S M and Boyd R W 2016 *Phys. Rev. Lett.* **116** 130402
[116] Bamber C and Lundeen J S 2014 *Phys. Rev. Lett.* **112** 070405
[117] Mirhosseini M, Magana-Loaiza O S, Chen C, Rodenburg B, Malik M and Boyd R W 2013 *Opt. Express* **21** 30196
[118] Bennett C and Brassard G 1984 *Proc. IEEE Int. Conf. CSSP* vol **175**
[119] Mirhosseini M, Malik M, Shi Z and Boyd R W 2013 *Nat. Commun.* **4** 2781

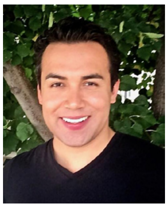

Omar S. Magaña-Loaiza received his B. S. from the Instituto Nacional de Astrofisica, Optica y Electronica in 2010. He received a Master and Ph.D. from the University of Rochester in 2012 and 2016, respectively. His doctoral dissertation was in the area of quantum coherence. He was a Research Associate in the Quantum Nanophotonics Group at the National Institute of Standards and Technology in Boulder from 2017 to 2018. He joined the faculty of Louisiana State University as an Assistant Professor of Physics in Fall of 2018. Now he leads the Experimental Quantum Photonics Group. His research group investigates novel properties of light and their potential for quantum technologies.

Robert Boyd was born in Buffalo, New York, USA. He received a BS degree in physics from MIT and a PhD in Physics from the University of California at Berkeley. He joined the faculty of the University of Rochester in 1977, where he is now a full professor. In 2010 he took in addition a faculty position at the University of Ottawa in Canada. His research involves both classical and quantum aspects of Nonlinear Optics. He is the recipient of the OSA Townes award and the APS Schawlow Award and the Isakson Award. He is a fellow of OSA, APS, SPIE, IEEE and AAAS. He is a fellow of the Royal Society of Canada and a corresponding member of the Heidelberg Academy.